

RICE UNIVERSITY

Search for Muonic Atoms at STAR

by

Kefeng Xin

Analysis Notes

Houston, Texas

Oct, 2014

1

ABSTRACT

2

Search for Muonic Atoms at STAR

3

by

4

Kefeng Xin

5 In ultrarelativistic heavy-ion collisions with high particle multiplicities, a produced
6 muon can be bound to a charged hadron (*proton, antiproton, K^+ , K^- , π^+ , π^-*) by
7 Coulomb force and form a hydrogen-like atom. Among these atoms, the antimatter
8 muonic hydrogen and the $K\text{-}\mu$ atom have been predicted but not yet been discovered.
9 For the STAR experiment, muon identification at low transverse momentum provides
10 a great opportunity to search for a variety of muonic atoms. As suggested by Melvin
11 Schwartz, Jack Sandweiss and many other theorists, muonic atoms can be an ideal
12 tool to determine the thermal emission from the Quark-Gluon Plasma via a direct
13 measurement of the single-muon spectra because only thermal muons or muons from
14 short-lived resonance decays are capable of forming such atoms.

Contents

16	Abstract	ii
17	List of Illustrations	v
18	1 Introduction	1
19	2 Dataset and Particle Selection	2
20	2.1 Data Set and Triggers	2
21	2.2 Track Selections	5
22	2.3 Particle Identification	7
23	3 Analysis and Results	12
24	3.1 Atom Production at STAR	12
25	3.2 Femtoscopic Correlations	14
26	3.2.1 $\pi\text{-}\mu$ Correlations	23
27	3.2.2 $\pi\text{-}\pi$ Correlations	24
28	3.3 Invariant Mass	31
29	3.3.1 Combinatorial Method	31
30	3.3.2 Invariant Mass Signal	37
31	3.4 Systematic Uncertainties	40
32	3.5 Atom Yield from Measurement	54
33	4 Theoretical Calculation with Measure Hadron and Lep-	
34	ton Yield	59

35 Bibliography 67

Illustrations

37	2.1 The vertex distribution along the Z-direction, measured from the	
38	TPC and the VPD detector.	4
39	2.2 Number of events.	5
40	2.3 Reference multiplicity distributions from central trigger events in	
41	AuAu200 collisions from Run 10.	7
42	2.4 Number of TPC hits, dE/dx hits, and nHits/nPossible distributions	
43	for primary muon candidates.	8
44	2.5 The $\Delta 1/\beta$ distribution for muons after TPC cut.	10
45	2.6 The $\Delta 1/\beta$ distribution for kaons and protons after TPC cut.	11
46	3.1 α distribution from the BNL (left) and Fermilab (right) K_l to $\pi\mu$	
47	atom experiment.	13
48	3.2 A sketch of a muonic atom event at STAR detector. An atom was	
49	produced right after freeze-out, and then it travels straight to the	
50	beam pipe. After the interaction with the beam pipe, the hadron and	
51	the muon are disassociated and detected in the TPC and the TOF. .	15
52	3.3 The effect from momentum shift is found to be a smaller than the bin	
53	size $2.5 MeV/c^2$. (Produced by Long Zhou).	16
54	3.4 The correlation functions calculated from $K\pi$ system [9]. In the $K\pi$	
55	system, the interactions are dominated by Coulomb interactions.	
56	From the figure, we see the interactions are stronger at low k^k and	
57	gets weaker at higher k^* where they have very different momentum. .	17

58	3.5 A sketch showing the case that particle 1 is produced closer to the center of the system, and travels faster than particle 2.	18
59		
60	3.6 The correlation functions for K - π pairs in AuAu200 GeV central triggered events.	20
61		
62	3.7 The correlation functions for K - μ pairs.	21
63		
64	3.8 Correlation function according to pair direction.	21
65		
66	3.9 The double ratio of the K - π and K - μ systems show significant difference at low k^* . The convergence to unity of K - μ suggests the ionization at the beam pipe after the production of muonic atoms. . .	22
67		
68	3.10 Measured π - μ correlation functions.	23
69		
70	3.11 Measured π - π correlation functions. In like-sign, the two contributions from Coulomb and quantum effect are mixed, and give the correlation function such structure.	24
71		
72	3.12 The simulation process for π - μ_A correlations. The dashed line represents the correlation between pions and muons from weak decays. .	25
73		
74	3.13 π - μ_A correlation functions.	26
75		
76	3.14 Three correlation functions.	27
77		
78	3.15 Check the linear relation between BC and AC . The black line is a linear fit to the data points.	28
79		
80	3.16 Measured π - μ correlation function, fitted by π - π correlation function and simulated π - μ_{decay}	31
81		
82	3.17 π - μ from data: measured π - μ correlation function; 1/C: reversed π - π correlation function; A: simulated π - μ_{decay}	32
83		
84	3.18 Measured π - μ correlation function, fitted by π - π correlation function and simulated π - μ_{decay} in a different fitting range shown in the figure.	33
85		
86	3.19 Measured π - μ correlation function, fitted by π - π correlation function and simulated π - μ_{decay} in a double binning x-axis shown in the figure.	33
87		

85	3.20 The raw counts of different types of hadron muon invariant mass distributions. SE stands for Same-Event; ME stands for Mixed-Event; LS stands for Like-Sign; the lower case letters p/n stands for the charge, positive/negative of the hadron and muons.	35
86		
87		
88		
89	3.21 The acceptance correction factors for atoms i.e. positive-negative pairs and anti atoms i.e. negative-positive pairs.	36
90		
91	3.22 The like-sign and mixed-event backgrounds are compared.	37
92		
93	3.23 Ratios in $K-\mu$ pairs. The red solid markers show the signal-to-background ratio from like-sign method; the blue empty makers show the signal-to-background ratio from mixed-event method; the black markers show the difference between the two methods.	39
94		
95		
96		
97	3.24 The difference between two background methods, normalized by mixed-event in $K-\mu$ pairs. The difference shows the Coulomb effect.	40
98		
99	3.25 The pair invariant mass signal-to-background distributions of $UL \times LS/ME^2 - 1$ show peaks at the atom masses.	41
100		
101	3.26 The $UL \times LS/ME^2 - 1$ distributions show peaks at the atom masses. The x-axis is the mass difference between the pair invariant mass and the sum of hadron and muon mass: $\delta m = m_{pair} - m_{hadron} - m_{muon}$	43
102		
103		
104	3.27 DCA variation.	43
105		
106	3.28 DCA variation.	44
107		
108	3.29 DCA variation.	45
109		
110	3.30 Cuts variation for both nHitsFit and nHitsDedx.	45
111		
112	3.31 DCA variation.	46
113		
114	3.32 Cuts variation for $1/\beta$	46
115		
116	3.33 Uncertainties from $1/\beta$ variations.	47
117		
118	3.34 Systematic uncertainties from all contributions.	47
119		
120	3.35 Mass signal, systematic uncertainties represented by shaded bands.	48
121		

113	3.36 DCA variation.	49
114	3.37 Differences between varied cuts and standard cut.	49
115	3.38 TOF cut variation.	50
116	3.39 Hit point variation.	50
117	3.40 Differences in hit point variation.	51
118	3.41 Total systematic uncertainties are from quadrature sum of contributions.	51
119		
120	3.42 Correlation functions for K - π and K - μ system, systematic uncertainties represented by shaded bands.	52
121		
122	3.43 Correlation functions for p - π and p - μ system,.	52
123		
124	3.44 Reduced mass scaling of the correlation function.	53
125		
126	3.45 Reduced mass scaling of the correlation function.	53
127		
128	3.46 The $UL \times LS/ME^2 - 1$ distribution for atoms from $K\pi$ pairs are used as residual background. The atom signal is shown in the shaded area after residual subtraction.	54
129		
130		
131	3.47 The $UL \times LS/ME^2 - 1$ distribution for antimatter atoms from $K\pi$ pairs are used as residual background. The atom signal is shown in the shaded area after residual subtraction.	55
132		
133	3.48 The mixed-event distributions for $K^+\mu^-$ and $K^-\mu^+$	55
134		
135	3.49 The $K\mu$ atoms and antimatter atom candidates	56
136		
137	3.50 Invariant mass distributions for proton- π pairs.	56
138		
139	3.51 The $UL \times LS/ME^2 - 1$ distribution for atoms from p - π pairs are used as residual background. The atom signal is shown in the shaded area after residual subtraction.	57
140		
	3.52 The $UL \times LS/ME^2 - 1$ distribution for antimatter atoms from p - π pairs are used as residual background. The atom signal is shown in the shaded area after residual subtraction.	57
	3.53 The muonic hydrogen and antimatter muonic hydrogen candidates .	58

¹⁴¹	4.1	μ^- phase space, weighted by $\frac{1}{2\pi p_{T\mu}}$	63
¹⁴²	4.2	K^+ phase space, weighted by $\frac{1}{2\pi p_{T\mu}}$	64
¹⁴³	4.3	Atom count distributions.	65
¹⁴⁴	4.4	Anti-atom count distributions.	66

145

Chapter 1

146

Introduction

147 Muonic atoms are like ordinary atoms except that the electrons are replaced with
 148 muons. These atoms have been studied in many fundamental physics experiments,
 149 such as precision measurements of proton size [1] and nuclear quadrupole moments [2].
 150 Muonic atoms with pions in the core have been produced from intense K_l beam at
 151 Brookhaven National Lab [3] and Fermilab [4]. However hydrogen-like muonic atoms
 152 with more exotic particles in the core (kaons or antiproton) have never been observed.
 153 Heavy-ion experiments, with large amount of thermal muons and hadrons produced,
 154 make an ideal environment for the production of such exotic atoms. This provides us
 155 a great opportunity to make these discoveries.

156 We present the search results for muonic atoms on $\sqrt{s_{NN}} = 200$ GeV Au+Au
 157 collisions collected by the STAR experiment at RHIC. With the muon identification
 158 at low momentum, the invariant mass spectra were reconstructed. Clear signals
 159 are observed at the expected atom masses. Two particle correlations show that the
 160 production of the daughter particles happens at the same space-time point, presenting
 161 the signature of atom ionization.

162

Chapter 2

163

Dataset and Particle Selection

164

2.1 Data Set and Triggers

165 The dataset used in this analysis is from Au+Au collisions at $\sqrt{s_{NN}} = 200$ GeV
 166 collected by the STAR detector in year 2010. Central triggered events are selected to
 167 maximize the particle multiplicities. This particular trigger is used to select events
 168 with high multiplicities from head-on collisions. Trigger IDs are 260101, 260103,
 169 260113, and 260123. More trigger information can be found at the webpage:

170 <http://www.star.bnl.gov/protected/common/common2010/trigger2010/streams.html>

171 The file catalog query for the input is

172 `catalog:star.bnl.gov?production=P10ik,sname2=st_physics,runnumber=&runnumber;,filetype=`
 173 `daq_reco_Mudst,tpx=1,sanity=1,storage=nfs" nFiles="all"`

174 The basic event QA has been done by Alexander Schmah and Hiroshi Masui. The
 175 bad run from the base QA are rejected. A full list of the bad runs can be found at
 176 <http://www.star.bnl.gov/cgi-bin/protected/cvsweb.cgi/offline/users/hmasui/StRefMultCorr/>
 177 `bad_runs.txt?rev=1.2`

178 Detailed plots are shown in the presentation below:

179 http://www.star.bnl.gov/protected/bulkcorr/hmasui/2011/Centrality_200GeV_Nov08/
 180 `hmasui_centrality_Run10_AuAu_200GeV_PWGC_Nov08_2011.pdf`

181 The complete bad run list is:

```

182 const Int_t bad_run_list_200GeV[219] = { 11002120, 11002121, 11002126, 11002127,
183     11002129, 11003010, 11003011, 11003101, 11003102, 11004007, 11004008, 11004009,
184     11004010, 11004011, 11004012, 11004013, 11004014, 11004015, 11004016, 11004018,
185     11004020, 11004021, 11004023, 11004024, 11004025, 11004026, 11004028, 11004029,
186     11004030, 11004032, 11004033, 11004034, 11004035, 11004037, 11004038, 11005042,
187     11006004, 11006005, 11006008, 11007015, 11010031, 11011019, 11011053, 11015069,
188     11015071, 11016024, 11017006, 11018003, 11018007, 11018008, 11018036, 11019001,
189     11019080, 11019081, 11021027, 11021028, 11021031, 11023048, 11025034, 11025038,
190     11025054, 11025067, 11025069, 11026005, 11026008, 11026021, 11026022, 11026023,
191     11026025, 11026067, 11026068, 11028004, 11028005, 11028006, 11028007, 11028008,
192     11028009, 11028010, 11028011, 11028012, 11028013, 11028018, 11028019, 11028020,
193     11028021, 11028022, 11028023, 11028024, 11028025, 11028026, 11028027, 11030041,
194     11030080, 11031061, 11031064, 11035008, 11035009, 11035072, 11036026, 11037035,
195     11037037, 11037060, 11037066, 11037067, 11038048, 11038049, 11038050, 11039047,
196     11039067, 11040078, 11040083, 11041022, 11041023, 11041040, 11041041, 11042001,
197     11042002, 11042003, 11042004, 11042005, 11042006, 11042007, 11042008, 11042011,
198     11042012, 11042018, 11042019, 11042020, 11042021, 11042022, 11042023, 11042024,
199     11042025, 11042026, 11042027, 11042042, 11042043, 11042044, 11042045, 11042046,
200     11042047, 11042048, 11042049, 11044029, 11047059, 11047065, 11047066, 11047067,
201     11048037, 11049001, 11049002, 11049005, 11049023, 11051038, 11051049, 11051051,
202     11051055, 11051063, 11051064, 11051068, 11052011, 11053057, 11054021, 11054022,
203     11054024, 11054059, 11054062, 11054066, 11057012, 11057035, 11057036, 11058005,
204     11058050, 11058083, 11059043, 11059055, 11059060, 11059075, 11059076, 11059077,
205     11060008, 11060049, 11060059, 11060069, 11060076, 11061008, 11061009, 11061021,
206     11061034, 11061037, 11061038, 11061095, 11063006, 11063007, 11063008, 11063011,
207     11063013, 11063014, 11063015, 11063016, 11063017, 11063036, 11063083, 11064003,
208     11064023, 11065038, 11066024, 11066045, 11071056, 11072032, 11072044, 11072045,
209     11073001, 11073002, 11073003, 11073049, 11075039, 11075045, 11075048 };

```

210 Events close to the center of the time-projection-chamber (TPC) along the beam

211 direction are selected by requiring $V_z(TPC) < 50$ cm. The measured vertex along

212 the beam direction (V_z) from the TPC has a strong relation with the measured V_z
from the VPD (See Fig. 2.1).

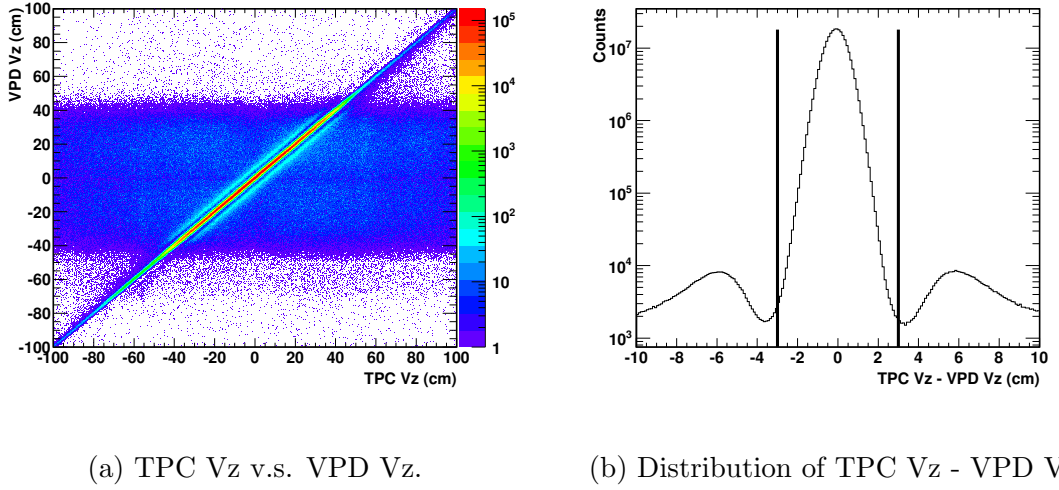


Figure 2.1 : The vertex distribution along the Z-direction, measured from the TPC
and the VPD detector.

213

214 To reject possible pileup events, for a same event the vertex Z measured from the
215 TPC and the VPD need to be close: $|Vz(TPC) - Vz(VPD)| \leq 3$ cm. Events that
216 are not at the center of the chamber on the X-Y plane are also rejected by requiring
217 $\sqrt{Vx^2 + Vy^2} < 2$ cm, where Vx and Vy are the transverse position with respect to
218 the center of the TPC. The event level cuts are listed in Tab. 2.1 Figure 2.2a shows
219 how the number of events changes when cuts are applied. Figure 2.2b shows the
220 number of events per trigger word. The reference multiplicity distribution is shown
221 in Fig. 2.3.

222 A total of 220 million events passed the event level selections.

Table 2.1 : Event Selection

Event Level Cuts
$V_z(TPC) < 50 \text{ cm}$
$ V_z(TPC) - V_z(VPD) \leq 3 \text{ cm}$
$\sqrt{V_x^2 + V_y^2} < 2 \text{ cm}$
$\text{refMult} \geq 20$

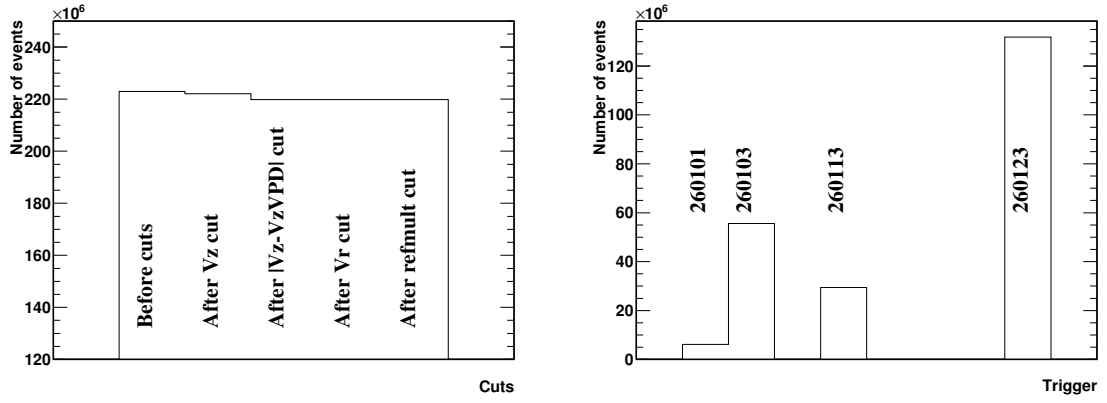


Figure 2.2 : Number of events.

2.2 Track Selections

²²³ General track quality cuts are listed in Tab. 2.2. The TPC hits distributions are

²²⁴ shown in Fig. 2.4

Table 2.2 : General track quality selections

Track Level Cuts
$GlobalDCA \leq 1 \text{ cm}$
$p_T^{primary} \geq 0.15 GeV/c$
$\eta < 1$
$Charge q == 1$
$nHitsFit \geq 20$
$nHitsDedx \geq 20$
$0.52 < nHitsFit/nHitsMax < 1.02$
$Y_{TOFLocal} < 1.8 \text{ cm}$

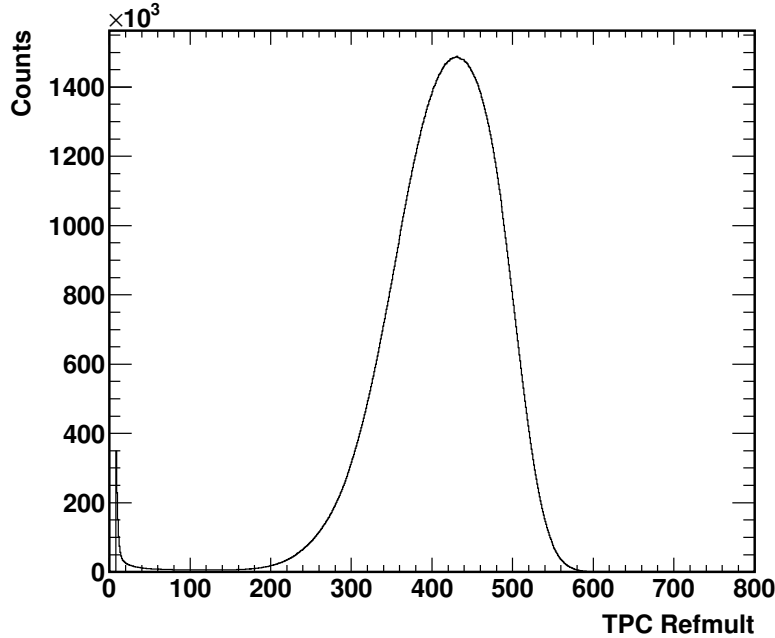


Figure 2.3 : Reference multiplicity distributions from central trigger events in AuAu200 collisions from Run 10.

²²⁶ 2.3 Particle Identification

²²⁷ Particles are identified based on energy loss measurement from the time projection chamber (TPC) and the timing measurement from the time-of-flight detector together. The muon momentum is limited to 0.15-0.25 GeV/c to ensure the purity of the sample. $-3 < n_{\sigma dE/dx} < -0.5$ cut is applied before TOF cuts, which

²³¹ we will discuss later. The normalized $\Delta 1/\beta$ distribution is calculated as follows:

$$\frac{\Delta \beta^{-1}}{\beta^{-1}} = \frac{\beta_{TOF}^{-1} - \beta_{TPC}^{-1}}{\beta_{TOF}^{-1}} = 1 - \beta \sqrt{1 - m^2/p^2},$$

where β_{TPC}^{-1} is the TPC measured β^{-1}

²³³ by assuming a mass m for a particular particle species. The $1/\beta$ distributions are

²³⁴ then fitted with two student-T distributions for each momentum slice in Fig. 2.5.

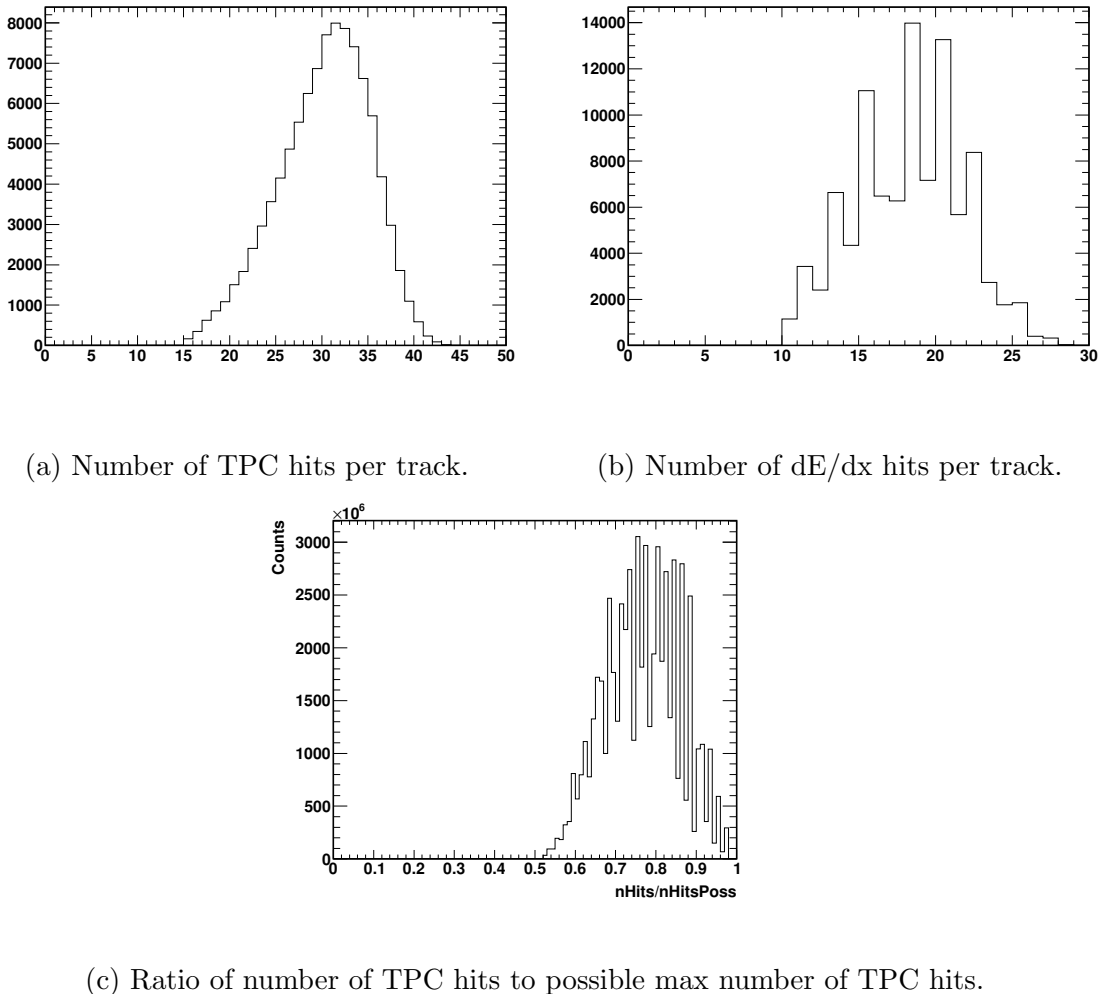


Figure 2.4 : Number of TPC hits, dE/dx hits, and $nHits/nPossible$ distributions for primary muon candidates.

235 Two Student T functions:

```

236   y = par[0]*(TMath:::Gamma((par[3]+1.0)/2.0)/(TMath:::Sqrt(par[3]*PI)*TMath:::Gamma(par
237       [3]/2.0)))*TMath:::Power(1.0+(t-par[1])*(t-par[1])/(par[3]*par[2]*par[2]),-(par[3]+1.0)
238       /2.0)) +
239       (par[4]*(TMath:::Gamma((par[7]+1.0)/2.0)/(TMath:::Sqrt(par[7]*PI)*TMath:::Gamma(par
240       [7]/2.0)))*TMath:::Power(1.0+(t-par[5])*(t-par[5])/(par[7]*par[6]*par[6]),-(par

```

241 [7] +1.0) / 2.0));

242 The lower limit is set to be -0.04, and the upper limit is set so that the purity of the
 243 sample, estimated from the fitting curves, is 99%. The upper limits are calculated for
 244 five momentum slices, evenly distributed from 0.15 - 0.25 GeV/c. Then a polynomial
 245 function of momentum is used to fit these upper limits. The obtained function is

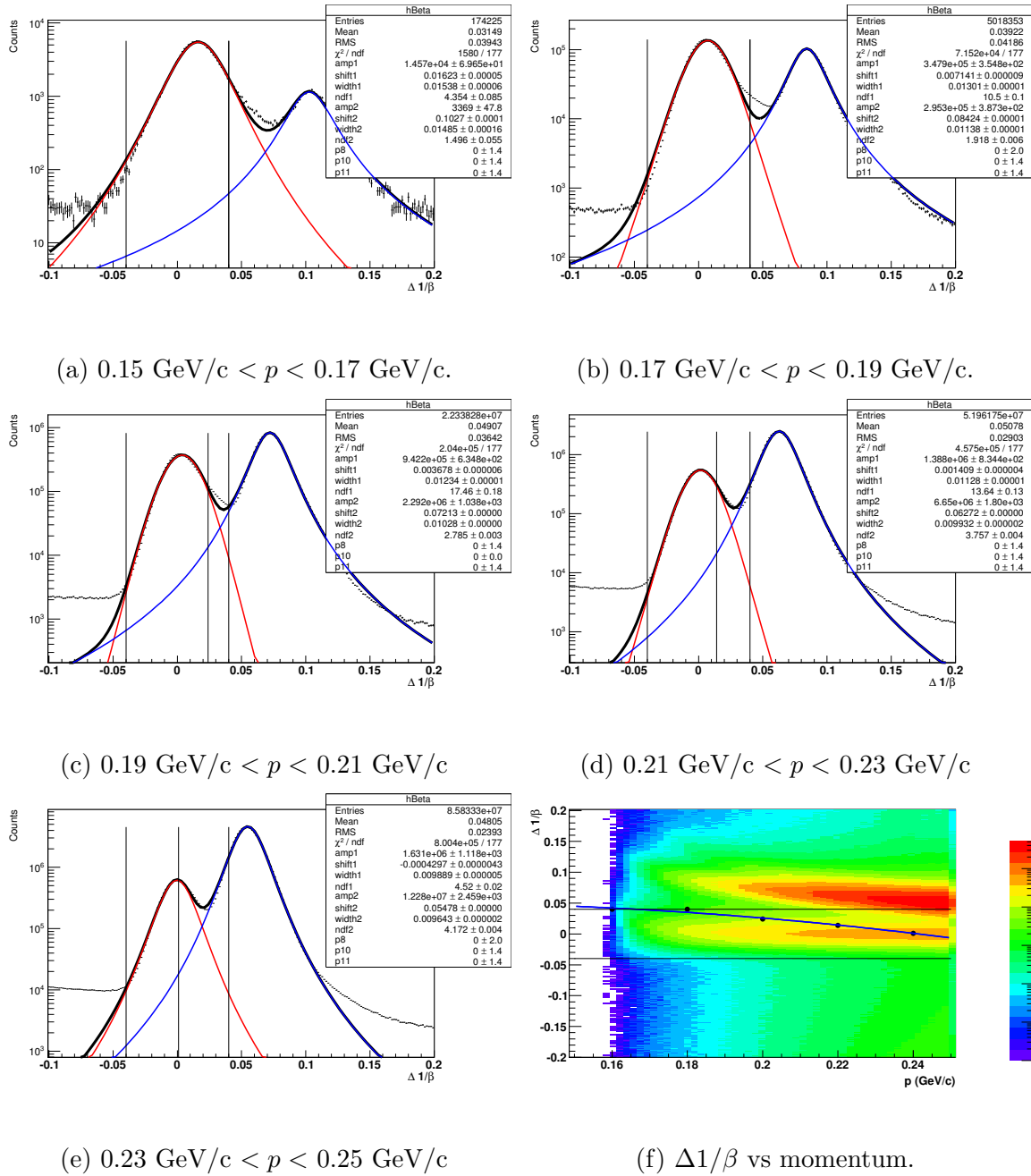
$$\Delta(1/\beta)_{upper\ limit}(p) = -2.64516 \times p^2 + 5.44703e^{-01} \times p + 2.26059e^{-02}, \quad (2.1)$$

246 as shown in the last panel of Fig. 2.5, represented by the curve. The tight cut at
 247 higher momentum (~ 0.22 GeV/c and above) is to insure the purity of the muon
 248 sample.

249 The distribution of the formed atom are found to be [5]

$$dN_{atom} = 8\pi^2\xi(3)m_{red}^2\alpha^3 \frac{dN_h}{p_{Th}dp_{Th}dy} \frac{dN_\mu}{p_{T\mu}dp_{T\mu}dy} p_{Tatom} dp_{Tatom} dy, \quad (2.2)$$

250 where the hardon, muon, and atom distributions are evaluated at the same rapidity
 251 and transverse momentum, so that $p_{atom}/m_a = p_h/m_h = p_\mu/m_\mu$. With this relation,
 252 the corresponding momenta for kaons and protons/antiprotons are 0.7-1.17 GeV/c
 253 and 1.33-2.22 GeV/c respectively. Fig. 2.6 shows the $\Delta 1/\beta$ distribution as a function
 254 of momenutm after $-3 < n\sigma_{dE/dx} < 3$ cut for kaons and protons. The upper cut is
 255 set to be 0.04, and the lower cut is set to be -0.04 if the purity is larger than 99%,
 256 except that at high momentum, where the purity of the sample between (-0.04, 0.04)
 257 is lower than 99%, the upper cut is then set base on 99% purity requirement. All the
 258 point for different momentum are then fitted with a polynomial function. The upper

Figure 2.5 : The $\Delta 1/\beta$ distribution for muons after TPC cut.

cuts as a function of momentum obtained from the fitting is expressed in Eq. 2.1.

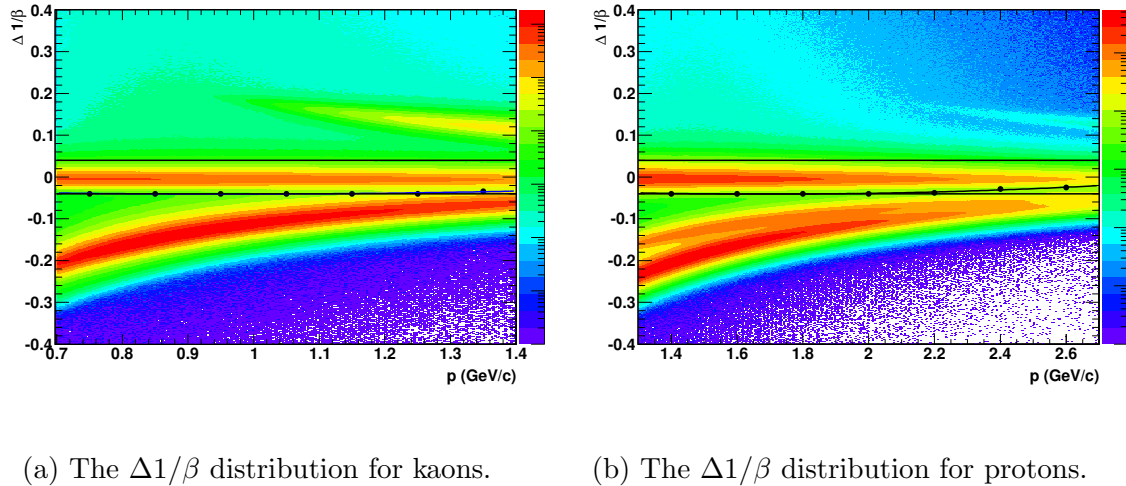


Figure 2.6 : The $\Delta 1/\beta$ distribution for kaons and protons after TPC cut.

260

Chapter 3

261

Analysis and Results

262 3.1 Atom Production at STAR

263 Previous experiments at Brookhaven National Lab [3] and Fermilab [4] have success-
 264 fully produced $\pi\text{-}\mu$ atoms from very intense K_l beam. Large amount of pions and
 265 muons are produced from K_l decays. When the produced π and K have similar veloc-
 266 ities, the Coulomb force bound them together as bound states and form $\pi\text{-}\mu$ muonic
 267 atoms. In these experiment, the atoms then pass a thin aluminum foil before the end
 268 of the vacuum channel. 0.030 inch thickness of the aluminum foil was calculated and
 269 was proved to be enough to ionize the atoms. The daughter pions and kaons then
 270 exit the foil at the same velocity and are filtered from background particles. The
 271 candidate events should pass all the filters, and form a sharp peak at $\frac{m_\pi - m_\mu}{m_\pi + m_\mu}$ in the
 272 α distributions, where $\alpha = \frac{p_\pi - p_\mu}{p_\pi + p_\mu}$. 33 events (BNL) and 320 candidates (Fermilab)
 273 were detected at the two experiments as shown in Fig. 3.1. This method, however
 274 cannot be used to produce other muonic atoms like $p\text{-}\mu$ or $K\text{-}\mu$.

275 In heavy-ion collisions at the STAR experiment, two gold nuclei are accelerated
 276 very close to the speed of light in opposite directions, and then collide. After the
 277 collision, a fireball of hot and dense matter with the degrees of freedom from quarks

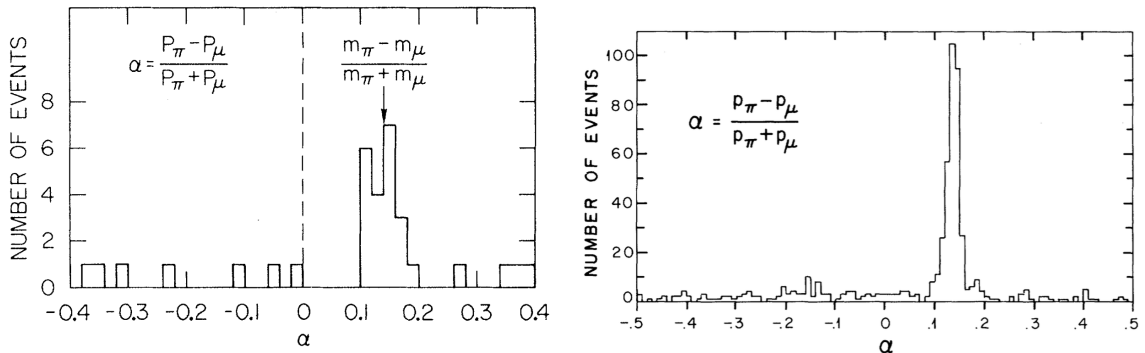


Figure 3.1 : α distribution from the BNL (left) and Fermilab (right) K_l to $\pi\text{-}\mu$ atom experiment.

and gluons are believed to be produced. Along with the expansion of the QCD matter, the temperature of the fireball drops and particles of many different species are produced. This process is called “freeze-out”. The atoms are predicted to be produced right after the particle freeze-out[5], which is of the order of a few fm (3-6 fm for pions). If the opposite charged particles have very similar velocities. Then a hadron can bind with a muon by the Coulomb force. The binding energies, which can easily be calculated from a hydrogen model with mass scaling, are a few KeV. The bound states, being neutral, travel in a straight line for a few centimeters, and then hit the beam pipe. The beryllium beam pipe at STAR serves as same purpose as the aluminum foil in the previous two experiments. This process is demonstrated in Fig. 3.2. The beam pipe is equivalent in terms of the radiation length to the aluminum foil, just enough to disassociate the hadron and the muon.

The V0-like decay length for muonic atoms are from the collision point to the

beam pipe, not exponentially distributed like strangeness particles such as K0s. If we put a centimeter decay length requirement for V0 reconstruction, we would loose too much statistics. Even for K0s, the reconstructing efficiency at very low pT is $\approx 1\%$. The distance between the primary vertex and the helix is 0.8mm in the worst case. The TPC does not have such resolution. The momentum shift from pointing the muon tracks back to the primary vertices was checked. A simulation is done to study the mass change from this momentum shift. Atoms were ionized at the beam pipe but daughter particles were reconstructed as primary tracks. The mass shift was found to be about $0.5MeV/c^2$ (Fig. 3.3), which is much less than the bin size ($2.5MeV/c^2$) we use in the next few sections.

3.2 Femtoscopic Correlations

Femtoscopic correlations between two particles can also be used as a probe of muonic atoms. The quantity k^* is defined as the magnitude of the momentum of either particle in the pair rest frame. The smaller the value of k^* is, the closer the two particles are in the phase space. The correlation function is defined as the ratio of the k^* distributions in the same event, where there is correlations, to the k^* distributions in the mixed event, where there is no correlations. The correlation as a function of k^* shows how the interactions of the two particles change with respect to their distance in phase space. STAR has thoroughly studied the $K-\pi$ system [9], in which only Coulomb interaction dominates. The correlation function of unlike-sign $K-\pi$ is

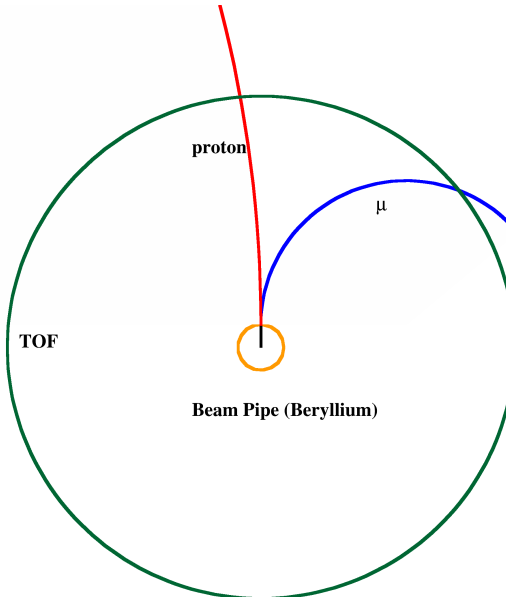


Figure 3.2 : A sketch of a muonic atom event at STAR detector. An atom was produced right after freeze-out, and then it travels straight to the beam pipe. After the interaction with the beam pipe, the hadron and the muon are disassociated and detected in the TPC and the TOF.

³¹¹ enhanced, approaching unity at higher k^* .

³¹² For non-identified particles, a leading particle can be selected. If the average
³¹³ space-time emission points of the two particle coincide, both correlation functions
³¹⁴ are identical. Then we have two scenarios. In the first scenario, the leading particle
³¹⁵ is produced closer to the center. If the leading particle travels faster than the pair,
³¹⁶ demonstrated in Fig. 3.5, this case is denoted as $C_+(k^*)$. The sign in the index is
³¹⁷ determined by the sign of $v_{pair} \cdot \vec{k}_\pi^*$. If the leading particle travels slower than the pair,

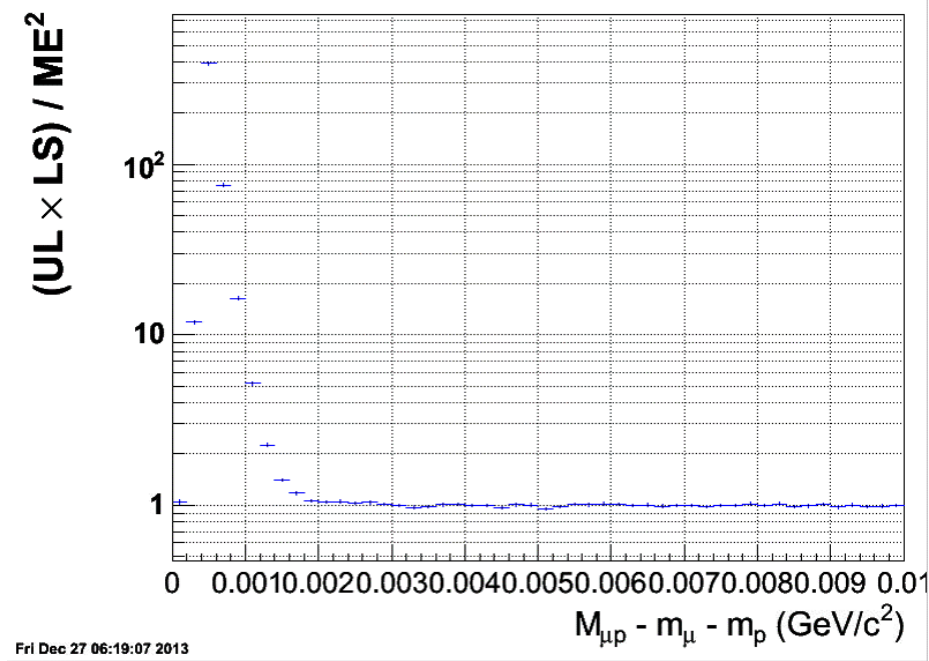


Figure 3.3 : The effect from momentum shift is found to be a smaller than the bin size $2.5 MeV/c^2$. (Produced by Long Zhou).

318 the sign of $\vec{v}_{pair} \cdot \vec{k}_\pi^*$ is negative, and this case is denoted as $C_-(k^*)$. In the first case,
 319 the leading particle tend to catch up with the other particle. The distance between
 320 them tends to be smaller and smaller, and the interactions tends to be enhanced.
 321 The correlations tends to be enhanced too. In the second case, the leading particle
 322 tends to move away from the other particle, and hence the correlations tends to be
 323 suppressed, due to similar reasons. Then in this scenario, the ratio of the correlation
 324 functions, $C_+(k^*)/C_-(k^*)$, so called the double ratio, must not be unity. And the
 325 deviation from unity must be similar as the correlation function $C(k^*)$ itself.

326 In the other scenario, the leading particle is produced further from the center than

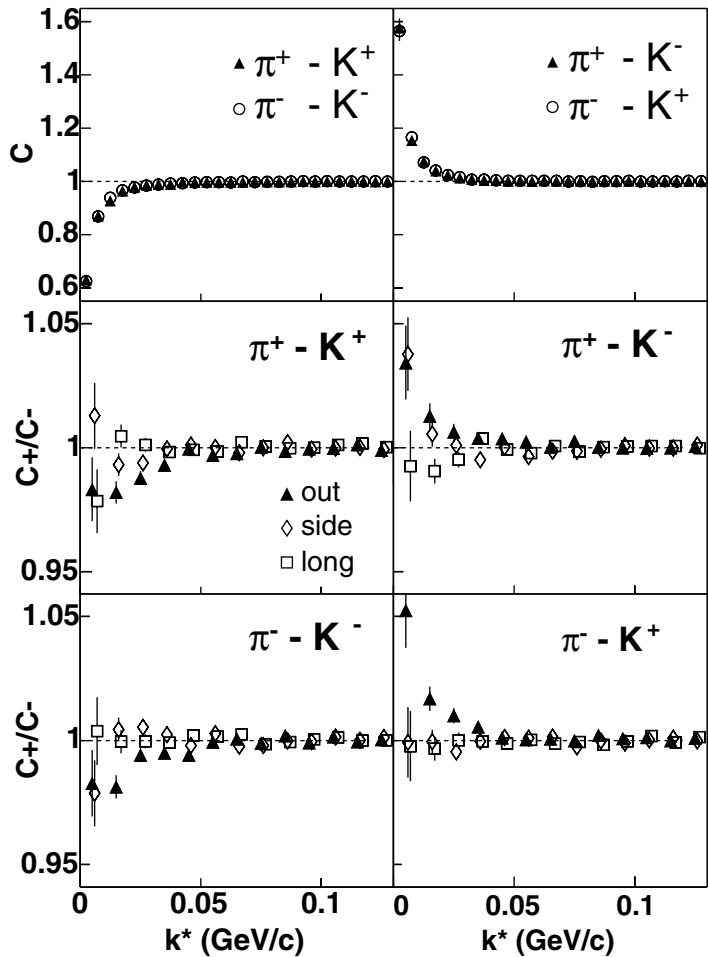


Figure 3.4 : The correlation functions calculated from K - π system [9]. In the K - π system, the interactions are dominated by Coulomb interactions. From the figure, we see the interactions are stronger at low k^k and gets weaker at higher k^* where they have very different momentum.

³²⁷ the other particle. If the leading particle travels faster, following the similar logic,
³²⁸ we know that $C_+(k^*)$ is calculated. However in this scenario, $C_+(k^*)$ is suppressed

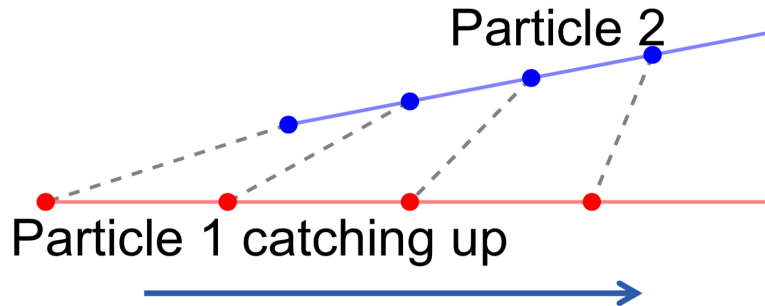


Figure 3.5 : A sketch showing the case that particle 1 is produced closer to the center of the system, and travels faster than particle 2.

³²⁹ because the two particles tend to move away. If the leading particle travels slower,
³³⁰ $C_-(k^*)$ is enhanced. So in this scenario, the double ratio $C_+(k^*)/C_-(k^*)$ also deviates
³³¹ from unity, but the trend, larger or smaller than unity, is different from the correlation
³³² function itself. This method was successfully used in previous measurements to probe
³³³ the space-time asymmetry of the emission of pions and kaons [9].

³³⁴ The correlation of the $K\pi$ system, as a reference to the $K\mu$ system, is calculated
³³⁵ from the dataset and kinetic region similar as $K\mu$ system which we used for muonic
³³⁶ atom signal extraction 3.6. The algorithm is as following. Tracks for a kaon and
³³⁷ a muon are first identified. Given the masses based on their particle species, their
³³⁸ Lorentz vectors (four-momentum vector) are saved for later use. The pair Lorentz
³³⁹ vector for each pair was calculated from the sum of the two. The kaon's, or equiva-
³⁴⁰ lently the muon's, Lorentz vector was then boosted to the pair rest frame according to
³⁴¹ the speed variable, which is the spatial components divided by the time component in

342 this vector. The magnitude of the three component of the kaon's or muon's Lorentz
 343 vector is k^* . The pseudo code is shown in below.

```
344 Algorithm for k* for pairs
345 -----
346 function fKstar ( particle1, particle2) // Lorentz vector for particle1 and particle 2
347     pair = particle1 + particle 2 // pair Lorentz vector
348     b = pair.mLorentz.BoostVector(); // b: 3 dimensional boost vector
349     particle1.Boost(-b) // boost into pair rest frame
350     v1 = particle1.vect // three vector for particle1
351     vpair = pair.vect // three vector for pair
352     If v1*vpair > 0 // inner product
353         sign = 1
354     else
355         sign = 0
356     return particle1.P()*sign // return k*
```

357 k^* distributions for same events are obtained by pairing all possible $K-\mu$ pairs within
 358 a given event. Mixed-event technique is similar as what has been used in the mass
 359 analysis. A event pool is generated by randomly selecting events and refreshing events
 360 in the pool as the data processing continues. When processing a new event, all kaon-
 361 s/muons in this event were paired with all kaons/muons from the event pool. As a
 362 result, the number of pairs from mixed events will be greater than the number of pairs
 363 from same events. This non-physics enhancement is treated by normalizing k^* dis-
 364 tributions at non-signal region. The scale factor is the ratio of integrated same-event
 365 k^* to mixed-event k^* . With the correlation functions $C(k^*)$ well defined, the double
 366 ratios C_+/C_- are calculated as described in The $K-\pi$ system shows enhancement in

367 double ratio from like-sign correlations, and suppression in double ratio from unlike-
 368 sign as expected. As we already know, the origin of the non-unity in double ratio
 369 comes from the Coulomb interactions between the kaons and pions, which are later
 370 on enhanced in $C_+(k^*)$ and suppressed in $C_-(k^*)$ because of the space-time emission
 371 asymmetries of kaons and pions.

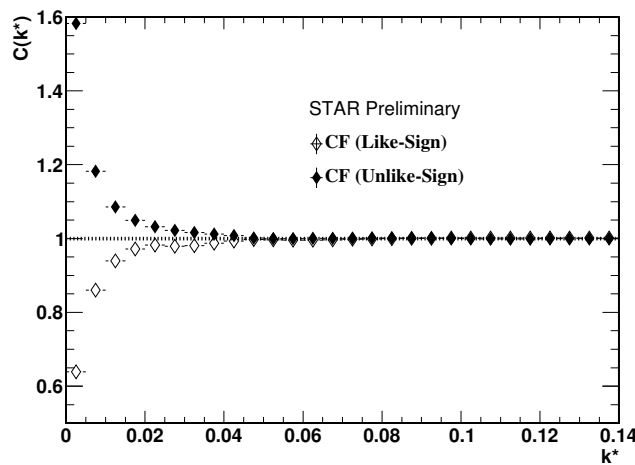


Figure 3.6 : The correlation functions for $K-\pi$ pairs in AuAu200 GeV central triggered events.

372 The correlation functions of $K-\mu$ system are shown in Fig. 3.7. The enhancement
 373 in unlike-sign pairs is observed; and the suppression in like-sign is observed. These
 374 indicate the attractive Coulomb force in unlike-sign pairs and repulsive Coulomb in
 375 like-sign pairs.

376 If picking a leading particle, the two cases can be separated and noted as C_+ and
 377 C_- , as shown in Fig. ??.

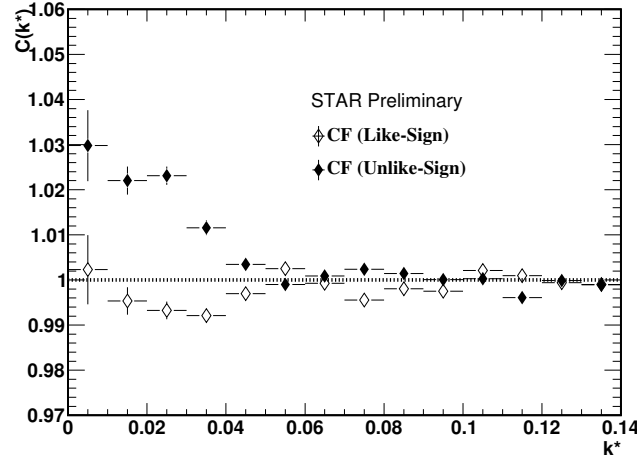
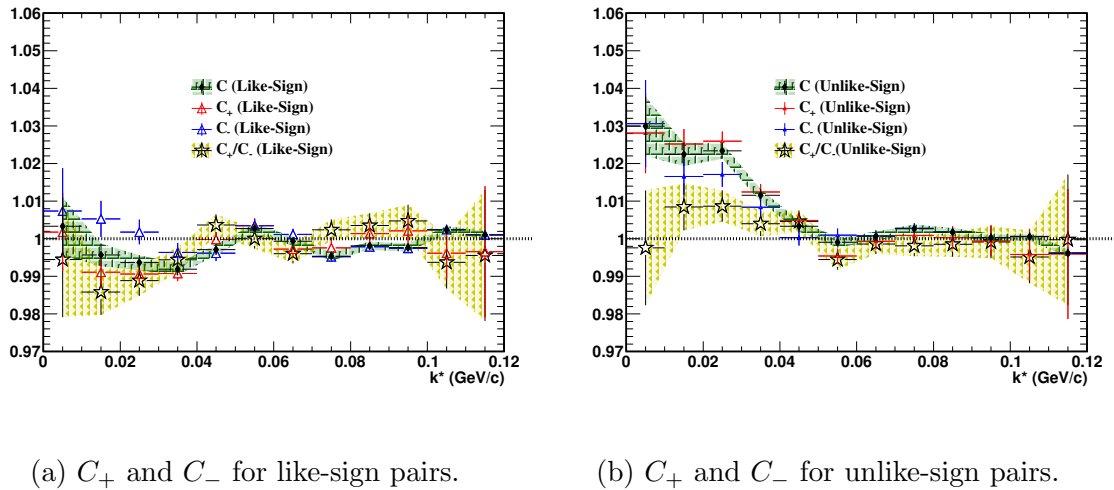


Figure 3.7 : The correlation functions for $K-\mu$ pairs.



(a) C_+ and C_- for like-sign pairs.

(b) C_+ and C_- for unlike-sign pairs.

Figure 3.8 : Correlation function according to pair direction.

378 The double ratio of $K - \mu$ system, overlaid on top of $K - \pi$ system, can be separated

379 in two regions as shown in Fig. 3.9. On the right of the dashed line, where only

380 Coulomb interactions are expected [9] in both systems, the double ratios of the two

381 systems are consistent. This is consistent with the existence of the Coulomb force,
 382 which is a necessary condition to form muonic atoms. On the left of the dashed
 383 line, where the muonic atoms are expected to appear, when getting to very low k^* ,
 384 instead of divergence, the double ratios of $K - \mu$ system show convergence to unity.
 385 The unity double ratio provides a signature of muonic atoms disassociation at the
 386 detector beam pipe, where the hadrons and the muons are separated from the bound
 387 state at the same space-time point.

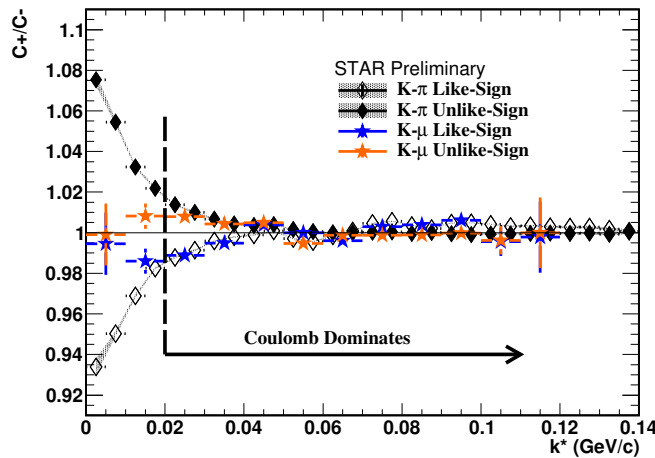


Figure 3.9 : The double ratio of the $K\pi$ and $K\mu$ systems show significant difference
 at low k^* . The convergence to unity of $K\mu$ suggests the ionization at the beam pipe
 after the production of muonic atoms.

³⁸⁸ **3.2.1 $\pi\text{-}\mu$ Correlations**

³⁸⁹ The $\pi\text{-}\mu$ correlations are studied to explore the interactions between pions and muons.

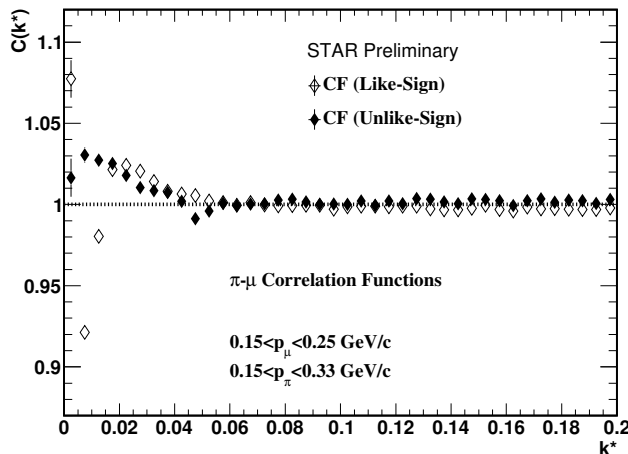


Figure 3.10 : Measured $\pi\text{-}\mu$ correlation functions.

³⁹⁰

³⁹¹ The enhancement of the correlation functions for like-sign pairs was observed.

³⁹² There should not be enhancement if there was only Coulomb interactions between π

³⁹³ and μ . The reason is that a large amount of muons from weak decays can pass the

³⁹⁴ track selections, and mix with the primordial muons. The $\pi\text{-}\pi$ correlation functions

³⁹⁵ were calculated in Fig. 3.11. The enhancement in like-sign pairs from identical particle

³⁹⁶ quantum effect is observed and agrees with previously published STAR results. [10].

³⁹⁷ **3.2.2 π - π Correlations**

³⁹⁸ The π - π correlations are also calculated to study the effect to π - μ correlations. In
³⁹⁹ Fig. 3.11, we observed the strong enhancement in like-sign, which comes from the quantum effect of identical particles.

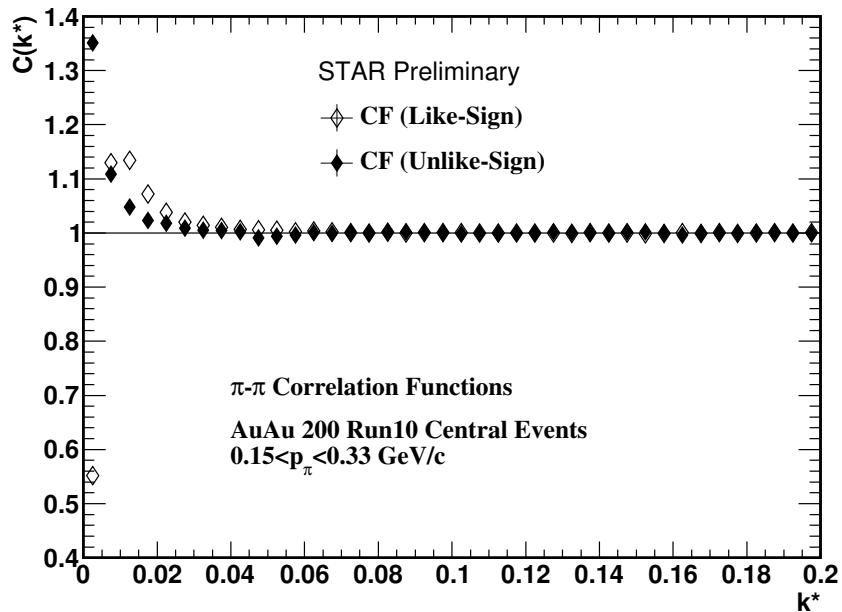


Figure 3.11 : Measured π - π correlation functions. In like-sign, the two contributions from Coulomb and quantum effect are mixed, and give the correlation function such structure.

⁴⁰⁰

⁴⁰¹ The measured π - μ correlation has two contributions. One is from the correlation
⁴⁰² between pions and primordial muons. The other is from the correlation between pions
⁴⁰³ and weak decay muons. The later can be simulated from real data. This process is
⁴⁰⁴ demonstrated in Fig. 3.12: one pion taken from the real data is decayed based on

405 energy momentum conservation. The artificial decayed μ is denoted as μ_A . Then
 406 we calculate the correlation function between this μ_A and another pion from the real
 data. The correlation functions of $\pi-\mu_A$ are shown in Fig. 3.13

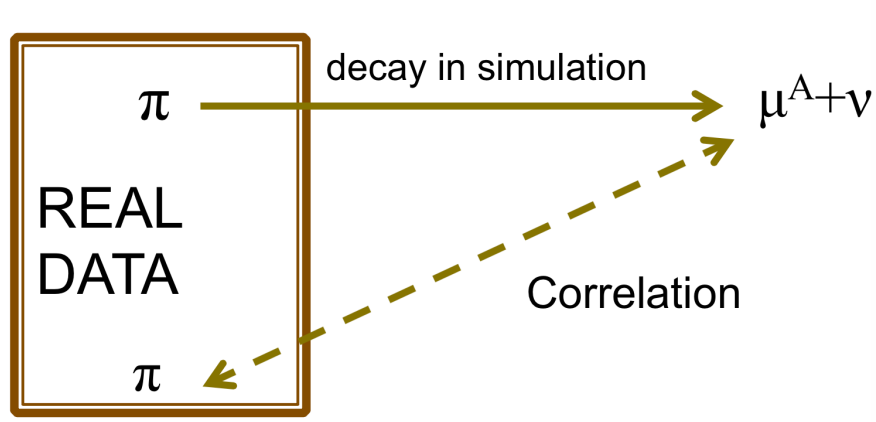


Figure 3.12 : The simulation process for $\pi-\mu_A$ correlations. The dashed line represents the correlation between pions and muons from weak decays.

407
 408 As a summary, these $\pi-\mu$ interactions inherit the interactions from $\pi-\pi$ inter-
 409 actions, which have two major sources, the electrostatic Coulomb interactions and
 410 quantum interference from identical pions. The later factor generates a strong en-
 411 hancement on the correlation functions. We denote the three correlation functions as
 412 the follows:

- 413 • A for correlations between pions and muons from simulated weak decays from
 414 real pions.
 415 • B for correlations between pions and inclusive muons, which is measured from

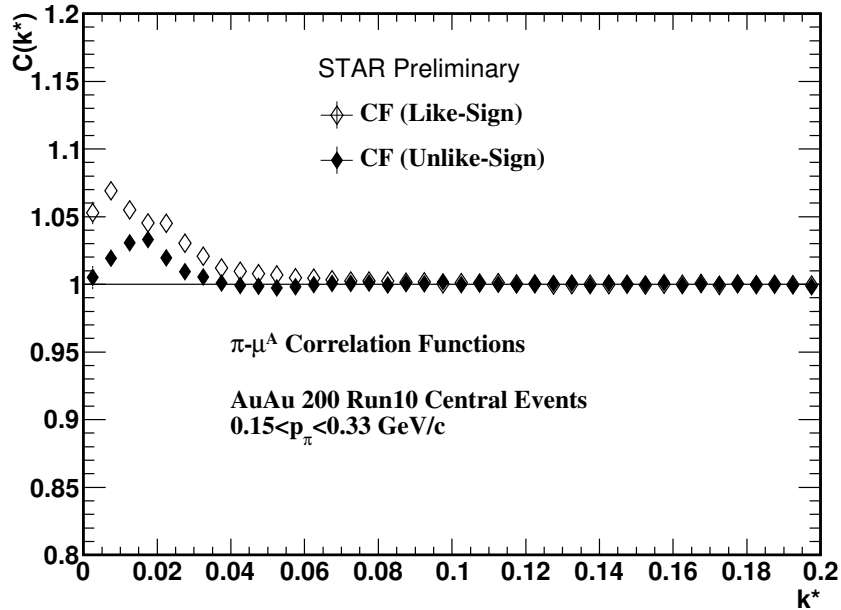


Figure 3.13 : $\pi-\mu_A$ correlation functions.

⁴¹⁶ data.

⁴¹⁷ • C' for correlations between pions and primordial muons.

⁴¹⁸ The three functions satisfy the linear relationship: $B = \alpha \times C' + \beta \times A$, where

⁴¹⁹ α stands for the fraction of primordial muons from inclusive muons produced from

⁴²⁰ the collisions. C' is then estimated by $\pi-\pi$ correlations, because of the fact that pion

⁴²¹ mass and muon mass are fairly close. To avoid quantum statistics enhancement, the

⁴²² correlation function from Coulomb between like-sign pairs is estimated from reversed

⁴²³ unlike-sign pairs C . The relationship then becomes:

$$B = \alpha \times 1/C + \beta \times A. \quad (3.1)$$

The three correlation functions are shown in Fig. 3.14.

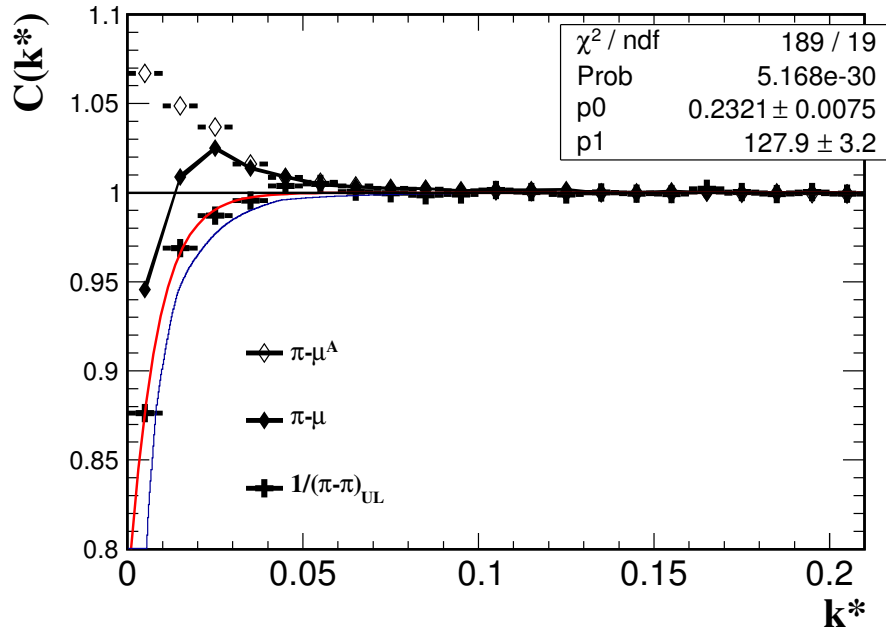


Figure 3.14 : Three correlation functions.

424

425 The relationship can be verified by checking if the following linear relationship
 426 holds: $B \times C = \alpha + \beta \times A \times C$. This relation is checked in Fig. 3.15, the red line
 427 represents a linear fit to the data points.

428 The minimum χ^2 fitting is performed in Fig. 3.16. In the fitting χ^2 is calculated
 429 from B 's uncertainty: $\chi^2 = \sum_i [(\beta \times A_i + \alpha \times 1/C_i - B_i)/\sigma_i]^2$. At the minimum point
 430 the partial derivatives of the function are zero:

$$\Rightarrow \begin{cases} \sum_i (\beta \times A_i + \alpha \times 1/C_i - B_i)/\sigma_i \times A_i/\sigma_i = 0 \\ \sum_i (\beta \times A_i + \alpha \times 1/C_i - B_i)/\sigma_i \times 1/C_i/\sigma_i = 0 \end{cases}$$

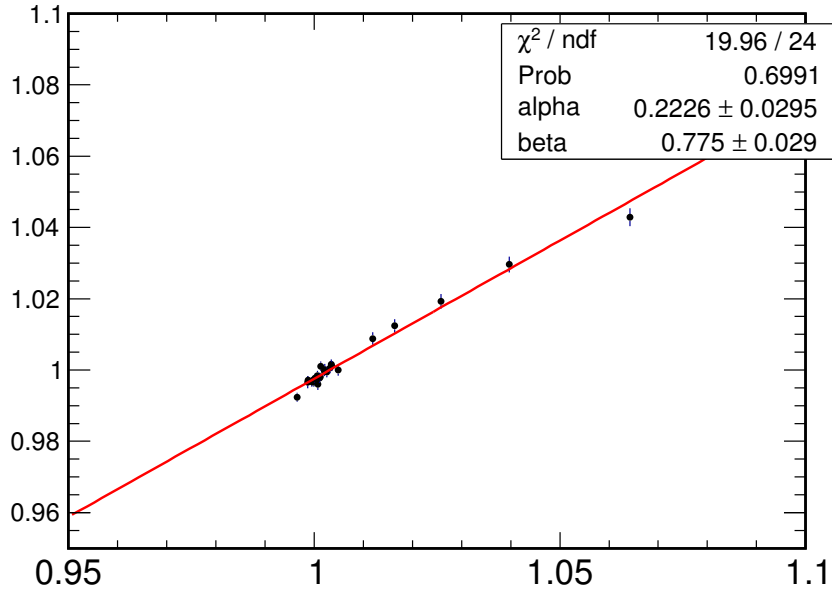


Figure 3.15 : Check the linear relation between BC and AC . The black line is a linear fit to the data points.

$$\Rightarrow \begin{cases} \alpha = \frac{\left(\sum_i \frac{A_i B_i}{\sigma_i^2}\right) \left(\sum_i \frac{1}{C_i^2 \sigma_i^2}\right) - \left(\sum_i \frac{B_i}{C_i \sigma_i^2}\right) \left(\sum_i \frac{A_i}{C_i \sigma_i^2}\right)}{\left(\sum_i \frac{A_i^2}{\sigma_i^2}\right) \left(\sum_i \frac{1}{C_i^2 \sigma_i^2}\right) - \left(\frac{A_i}{C_i \sigma_i^2}\right)^2} \\ \beta = \frac{\left(\sum_i \frac{A_i}{C_i \sigma_i^2}\right) \left(\sum_i \frac{A_i B_i}{\sigma^2}\right) - \left(\sum_i \frac{A_i^2}{\sigma_i^2}\right) \left(\sum_i \frac{B_i}{C_i \sigma_i^2}\right)^2}{\left(\sum_i \frac{A_i}{C_i \sigma_i^2}\right)^2 - \left(\sum_i \frac{A_i^2}{\sigma_i^2}\right) \left(\sum_i \frac{1}{C_i^2 \sigma_i^2}\right)} \end{cases}$$

⁴³¹ where the index i means each data points. The fitting errors are then propagated

⁴³² from the three quantities:

$$\left\{ \begin{array}{l} \delta\alpha = \sqrt{\sum_i (\frac{\partial\alpha}{\partial B_i} \delta B_i)^2 + \sum_i (\frac{\partial\alpha}{\partial A_i} \delta A_i)^2 + \sum_i (\frac{\partial\alpha}{\partial C_i} \delta C_i)^2} \\ \delta\beta = \sqrt{\sum_i (\frac{\partial\beta}{\partial B_i} \delta B_i)^2 + \sum_i (\frac{\partial\beta}{\partial A_i} \delta A_i)^2 + \sum_i (\frac{\partial\beta}{\partial C_i} \delta C_i)^2} \end{array} \right.$$

⁴³³ From Eq. 3.1 we get:

$$\left\{ \begin{array}{l} \alpha = B - \beta AC \\ \beta = \frac{B - \alpha/C}{A} \end{array} \right.$$

⁴³⁴ Then these partial derivatives are:

$$\left\{ \begin{array}{l} \frac{\partial\alpha}{\partial A} = -\beta C, \\ \frac{\partial\alpha}{\partial B} = 1, \\ \frac{\partial\alpha}{\partial C} = -\beta A, \\ \frac{\partial\beta}{\partial A} = -\alpha C, \\ \frac{\partial\beta}{\partial B} = 1/A, \\ \frac{\partial\beta}{\partial C} = -\alpha/A, \end{array} \right.$$

⁴³⁵ Substitute these to Eq. 3.2:

$$\Rightarrow \begin{cases} \delta\alpha = \sqrt{\sum_i (\delta B_i)^2 + \sum_i (-\beta C_i \delta A_i)^2 + \sum_i (-\beta A_i \delta C_i)^2} \\ \delta\beta = \sqrt{\sum_i (1/A_i \delta B_i)^2 + \sum_i (-\alpha C_i \delta A_i)^2 + \sum_i (-\alpha A_i \delta C_i)^2} \end{cases}$$

⁴³⁶ Note that the particle tracks suffer from track merging when they are constructed
⁴³⁷ from the time projection chamber. If two particles have similar trajectories and ori-
⁴³⁸ entation, implying that they are close in momentum space, the detector will not be
⁴³⁹ able to have enough spacial resolution to distinguish them and will merge the two
⁴⁴⁰ tracks. When the simulated pion-to-muon decays are performed, the missing pions
⁴⁴¹ from track merging cannot be saved by any means. The fitting range is selected
⁴⁴² between 0.02-0.20 GeV/c, discarding the very low k^* where the missing track prob-
⁴⁴³ lem is significant. The fitting results show that the fraction of primordial muons is
⁴⁴⁴ $22.0 \pm 0.4\%$ in Fig. 3.16.

⁴⁴⁵ Figure 3.17 shows the measured correlation, the two fitting components, and the
⁴⁴⁶ fitting results altogether.

⁴⁴⁷ We also vary the fitting range at higher k^* to check if the fitting changes if we set
⁴⁴⁸ a high k^* limit. The fitting results are shown in Fig. 3.18. The difference of the two
⁴⁴⁹ will be taken into account into systematic uncertainties.

⁴⁵⁰ We also vary different binning method k^* to check if the fitting changes. The
⁴⁵¹ fitting results are shown in Fig. 3.19. The difference of the two will be taken into
⁴⁵² account into systematic uncertainties.

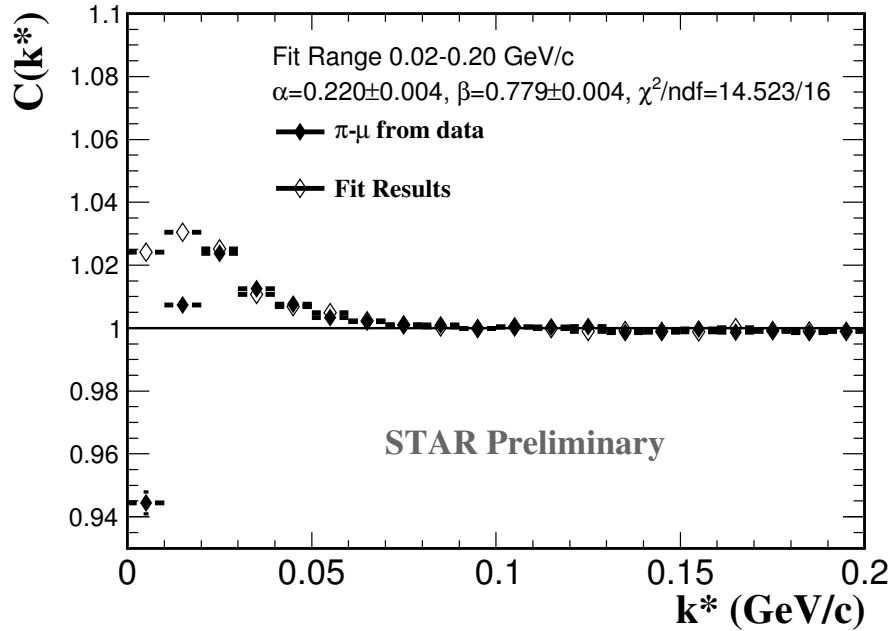


Figure 3.16 : Measured $\pi\mu$ correlation function, fitted by $\pi\pi$ correlation function and simulated $\pi\mu_{\text{decay}}$.

453 3.3 Invariant Mass

454 3.3.1 Combinatorial Method

455 The invariant mass reconstruction is done with the combinatorial method. The com-
 456 binatorial signal is constructed by pairing a hadron and a muon with opposite electric
 457 charges (unlike-sign method) from the same event. The background is constructed
 458 in two ways: a mixed-event method, in which a hadron and a muon with opposite
 459 electric charges from two different events are paired; and a like-sign method, in which
 460 a hadron and a muon with the same electric charge from a same event are paired.

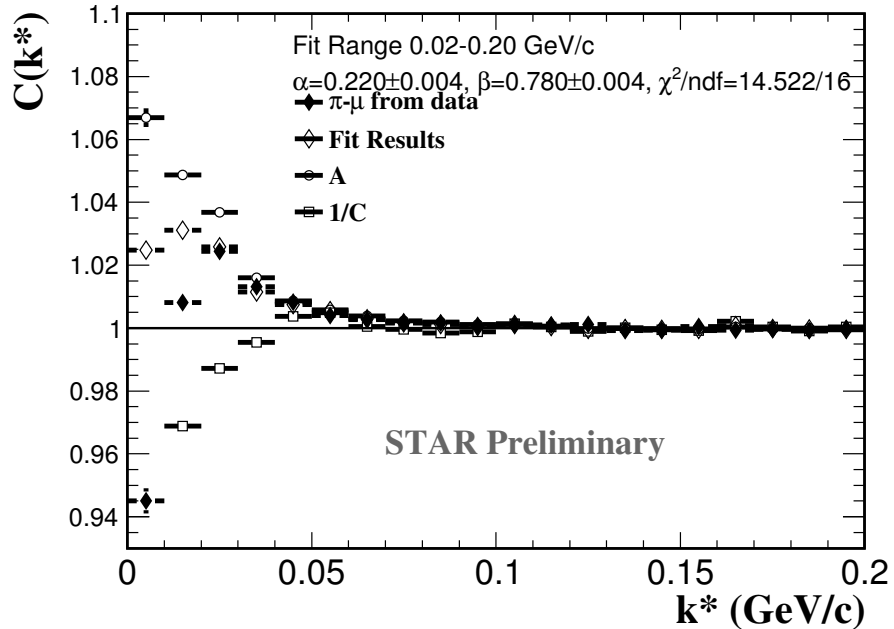


Figure 3.17 : $\pi\mu$ from data: measured $\pi\mu$ correlation function; $1/C$: reversed $\pi\pi$ correlation function; A: simulated $\pi\mu_{\text{decay}}$.

461 Events with different vertices pass different geometry of the detector. Thus only
 462 events with similar vertex positions should be mixed. We make 20 slices along the
 463 Z-direction between -50 to 50 cm, and only mixed events that fall into the same slice.
 464 Also we require events measured at the same magnetic field to be mixed. We do not
 465 require a multiplicity selection since the events are from central trigger. The distribu-
 466 tions from mixed events are then need to be normalized [7, 8]. The equations are also
 467 shown in Eq. 3.2 to 3.9, where SE represent the pair distributions from same events,
 468 and ME represent the pair distributions from mixed events. These distributions are
 469 functions of pair invariant mass, i.e. $m_{h\mu}$. When performing normalization, the ratio

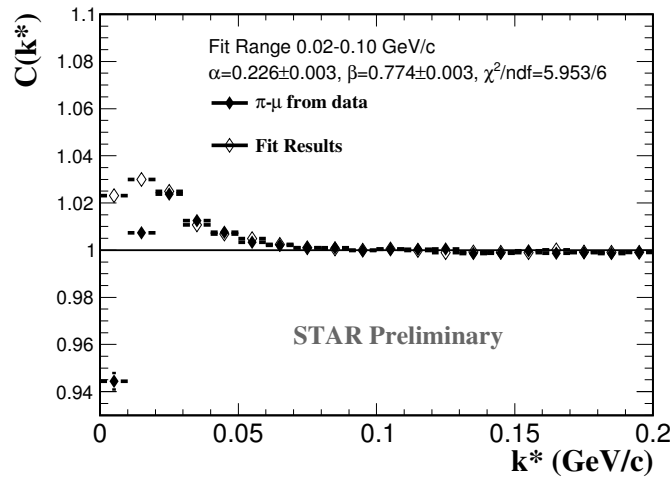


Figure 3.18 : Measured $\pi\text{-}\mu$ correlation function, fitted by $\pi\text{-}\pi$ correlation function and simulated $\pi\text{-}\mu_{\text{decay}}$ in a different fitting range shown in the figure.

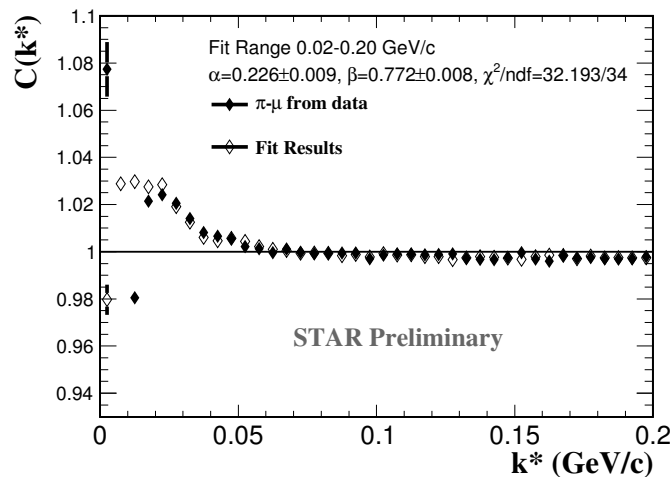


Figure 3.19 : Measured $\pi\text{-}\mu$ correlation function, fitted by $\pi\text{-}\pi$ correlation function and simulated $\pi\text{-}\mu_{\text{decay}}$ in a double binning x-axis shown in the figure.

⁴⁷⁰ of integrated SE and ME over the normalization region (N. R.) is used.

$$A_{++} = \frac{\int_{N.R.} SE_{++}(m_{h+\mu+}) dm_{h+\mu+}}{\int_{N.R.} ME_{++}(m_{h+\mu+}) dm_{h+\mu+}} \quad (3.2)$$

$$A_{+-} = \frac{\int_{N.R.} SE_{+-}(m_{h+\mu-}) dm_{h+\mu-}}{\int_{N.R.} ME_{+-}(m_{h+\mu-}) dm_{h+\mu-}} \quad (3.3)$$

$$A_{-+} = \frac{\int_{N.R.} SE_{-+}(m_{h-\mu+}) dm_{h-\mu+}}{\int_{N.R.} ME_{-+}(m_{h-\mu+}) dm_{h-\mu+}} \quad (3.4)$$

$$A_{--} = \frac{\int_{N.R.} SE_{--}(m_{h-\mu-}) dm_{h-\mu-}}{\int_{N.R.} ME_{--}(m_{h-\mu-}) dm_{h-\mu-}} \quad (3.5)$$

$$ME_{++} = A_{++} \times ME_{++} \quad (3.6)$$

$$ME_{+-} = A_{+-} \times ME_{+-} \quad (3.7)$$

$$ME_{-+} = A_{-+} \times ME_{-+} \quad (3.8)$$

$$ME_{--} = A_{--} \times ME_{--} \quad (3.9)$$

⁴⁷¹ The invariant mass of varius types of hadron-muon pairs are calculated. The raw
⁴⁷² count distributions are shown in Fig. 3.20.

⁴⁷³ In like-sign method, the acceptance difference between like-sign and unlike-sign
⁴⁷⁴ need to be corrected. In the magnetic field, the particles with opposite charges bend
⁴⁷⁵ to different directions. The TPC has certain blind spots at sector boundaries or
⁴⁷⁶ dead sectors. These blind spots causes the loss of tracks, which is different for tracks
⁴⁷⁷ with different charges, i.e. different bending directions. When we pair two tracks,
⁴⁷⁸ the pairs with certain opening angles are lost more than others, leading to different
⁴⁷⁹ loss in different mass region. For like-sign and unlike-sign pairs, the lost on the

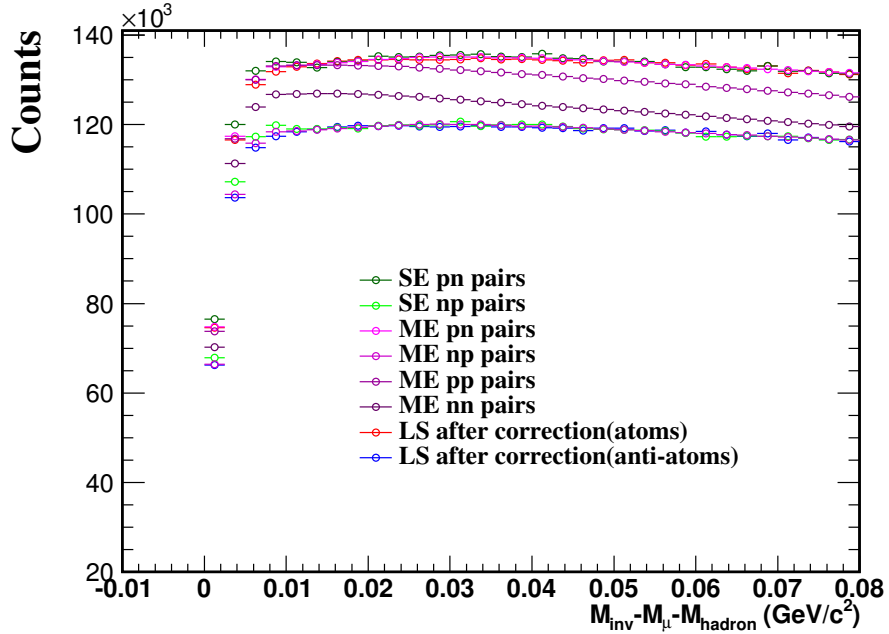


Figure 3.20 : The raw counts of different types of hadron muon invariant mass distributions. SE stands for Same-Event; ME stands for Mixed-Event; LS stands for Like-Sign; the lower case letters p/n stands for the charge, positive/negative of the hadron and muons.

480 opening angles are different leading to different loss in mass spectra. The mixed-event
 481 backgrounds are used for acceptance correction of like-sign backgrounds. Details of
 482 this correction are discussed in [7, 8]. The acceptance correction factor is the ratio of
 483 unlike-sign and like-sign pairs in mixed-event, i.e. $\frac{ME_{+-}}{\sqrt{ME_{++}ME_{--}}}$ for atoms. Then
 484 the geometry mean $\sqrt{LS_{++}LS_{--}}$ of the like-sign in same event are corrected by this
 485 factor to get the corrected like-sign background:

$$LS_{+-}(\text{corrected}) = \sqrt{LS_{++}LS_{--}} \frac{ME_{+-}}{\sqrt{ME_{++}ME_{--}}}, \quad (3.10)$$

⁴⁸⁶ where LS and ME stands for like-sign and mixed-event respectively, and the index
⁴⁸⁷ stands for the charges for hadrons and leptons. Similarly the corrected like-sign
⁴⁸⁸ background for antimatter atoms is:

$$LS_{-+}(\text{corrected}) = \sqrt{LS_{++}LS_{--}} \frac{ME_{-+}}{\sqrt{ME_{++}ME_{--}}}, \quad (3.11)$$

⁴⁸⁹ The acceptance correction factors for positive-negative pairs and negative-positive
pairs are shown show in Fig. 3.21.

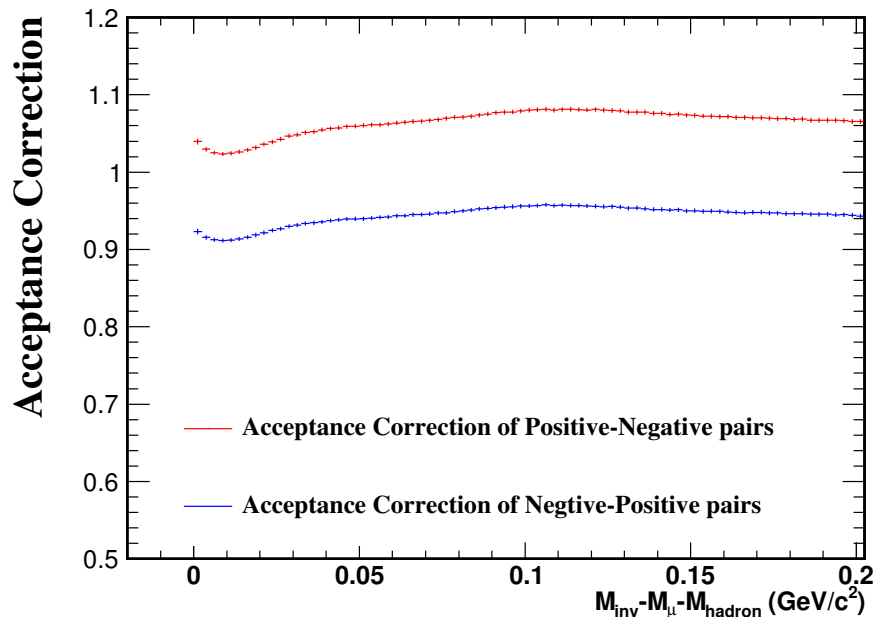


Figure 3.21 : The acceptance correction factors for atoms i.e. positive-negative pairs
and anti atoms i.e. negative-positive pairs.

⁴⁹⁰

⁴⁹¹ After the acceptance correction, the two backgrounds are compared in Fig. 3.22,
⁴⁹² and are found to be roughly consistent.

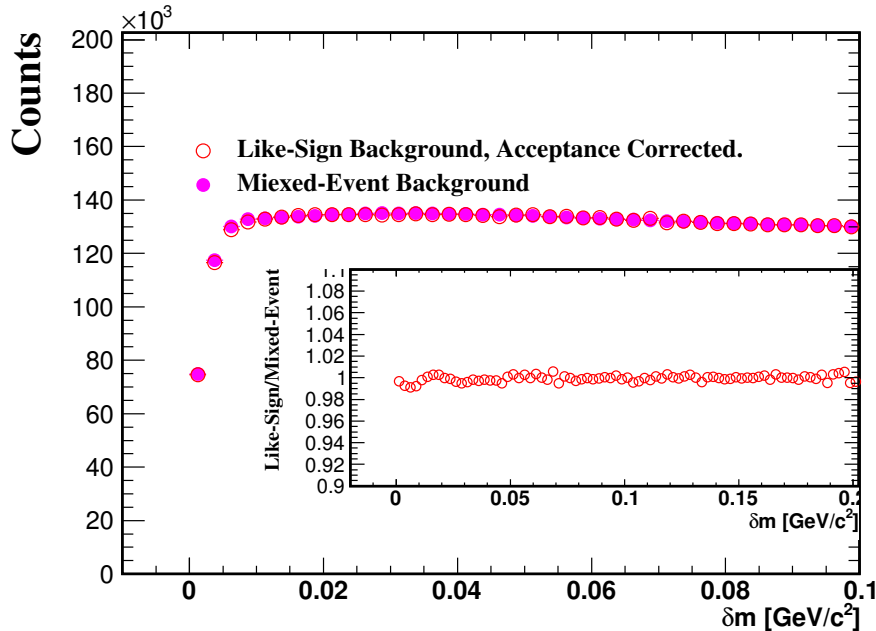


Figure 3.22 : The like-sign and mixed-event backgrounds are compared.

493 3.3.2 Invariant Mass Signal

494 The peak from the two daughter particles are expected to appear 0 net mass, i.e.
 495 $M_{pair} - M_\mu - M_{hadron} = 0 \text{ GeV}/c^2$. Because the binding energy is only about 3 KeV,
 496 which can be calculated by solving the Schrödinger equation of a hydrogen-like atom
 497 analytically. And when the atoms are ionized at the beam pipe, the binding energy
 498 is compensated by the excitation from atom-beam pipe interaction. In Fig. 3.23, the
 499 red markers show the signal-to-background ratio from the like-sign method, and the
 500 blue markers show the signal-to-background ratio from mixed-event method. Sharp
 501 peaks are observed at zero net mass for both methods. From this figure, we can see
 502 that the signal-to-background ratio extracted from like-sign method is systematically

503 higher than the signal extracted from mixed-event method. This is explained by
 504 the Coulomb effect. Note that the Coulomb effect becomes stronger when the two
 505 charged particles are close in phase space. In the unlike-sign method, two particles
 506 carry opposite charges, which produce attractive Coulomb force and thus enhance
 507 the mass distributions (larger than if there were no Coulomb), especially at the low
 508 mass region. In contrast, in the like-sign method, the repulsive Coulomb force from
 509 the same charge suppresses the mass distributions at the low mass region. In the
 510 mixed-event method, there is no Coulomb effect for hadron-muon pairs. When the
 511 signal-to-background ratio is calculated, like-sign is subtracted from the foreground
 512 and the results gets enhanced compared to mixed-event. The difference of the two
 513 methods are shown by the black markers in Fig. 3.24. We can see a clear region at
 514 low δm is above 0, and the integral along x-axis is 0.366, also above 0, which reveals
 515 the Coulomb effect between like-sign pairs.

516 Similarly, the signal to background ratio and background difference for $p-\mu$ are
 517 shown in Fig. 3.25. The $p-\mu$ possibly has additional contributions from hadronic
 518 resonance decay like $\Delta \rightarrow p + \pi \rightarrow p + \mu + \nu$, and thus is more complicated.

519 As discussed previously, the Coulomb effect in like-sign pairs and unlike-sign pairs
 520 has opposite effect on the mass distribution. The product of the two cases can cancel
 521 Coulomb effect. The following observable is adopted to cancel the Coulomb effect
 522 and preserve the signal:

$$UL \times LS/ME^2 - 1 \quad (3.12)$$

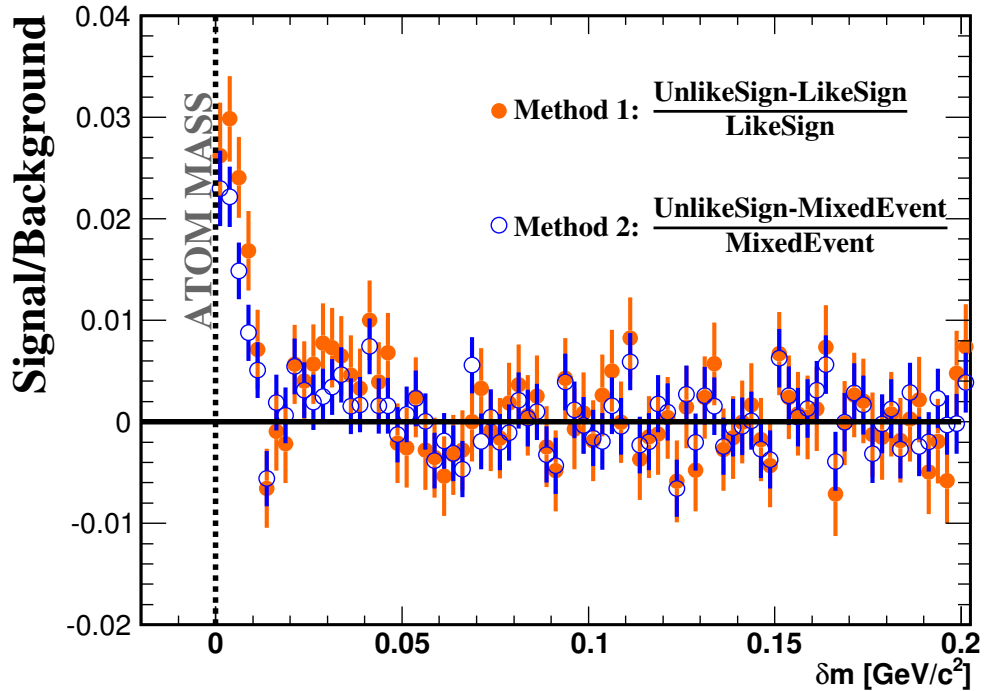


Figure 3.23 : Ratios in $K\mu$ pairs. The red solid markers show the signal-to-background ratio from like-sign method; the blue empty makers show the signal-to-background ratio from mixed-event method; the black markers show the difference between the two methods.

523 where $UL \times LS$ stands for unlike-sign \times like-sign, to cancel the Coulomb effect, and
 524 ME stands for mixed-event for normalization. After the rejection of the Coulomb
 525 force, this observable is the signal-to-background ratio from muonic atoms. We ob-
 526 serve the sharp peaks at the zero net mass in Fig. 3.26. The error bars show the
 527 statistical uncertainties. The signal is consistent in both $K\mu$ and $p\mu$ systems and
 528 their antimatter systems. The distribution at higher mass is relatively flat and consis-

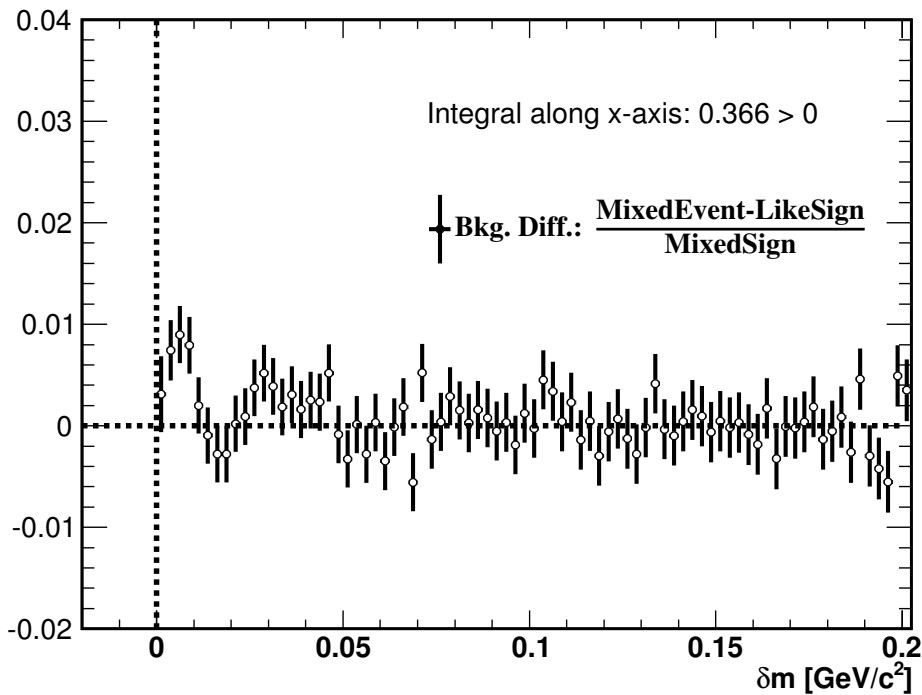
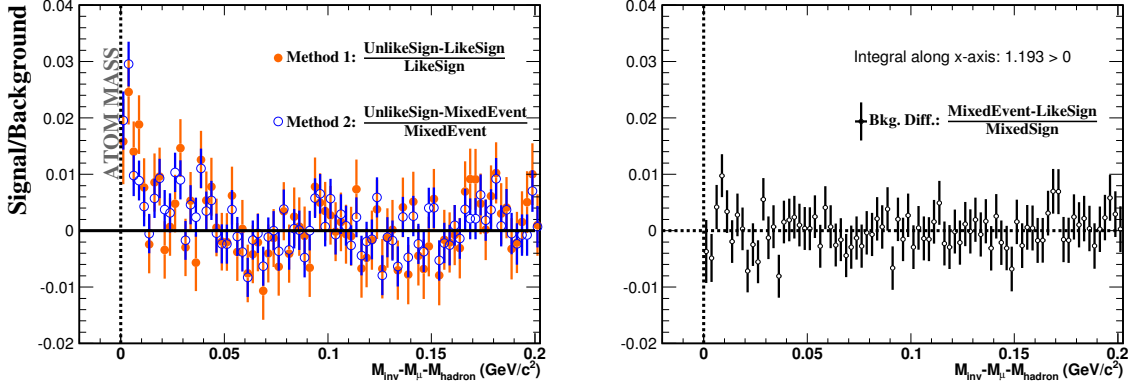


Figure 3.24 : The difference between two background methods, normalized by mixed-event in K - μ pairs. The difference shows the Coulomb effect.

529 tent with 0, indicating a good background determination from the methods described
530 above.

531 3.4 Systematic Uncertainties

532 The systematic uncertainties were estimated from varying cut selections. If the
533 dataset is large enough, it would have been a better approach so that the data can be
534 separated to two datasets with no overlap data, and the systematic uncertainties can
535 be estimated from the difference of the two independent analyses. The differences



(a) The signal to background ratio from like-sign method and sign method and mixed-event method for K - mixed-event method for $p-\mu^+$ pairs.
 μ^+ pairs.

Figure 3.25 : The pair invariant mass signal-to-background distributions of $UL \times LS/ME^2 - 1$ show peaks at the atom masses.

536 among the data from different cuts were combined to get a total uncertainty. The
 537 cuts that were studied include Distance of Closest Approach (DCA) between tracks
 538 and primary vertices, TPC hit points (nHitsFit), TOF PID cut, TPC energy loss
 539 points (nHitsDedx). Because the TPC hit point cuts, i.e. nHitsFit and nHitsDedx
 540 are positively correlated. Changing one cut will implicitly change the other cut. So
 541 the these two cuts are changed at the same time, and to the same direction, either
 542 increased or decreased. A detailed list of these cuts can be found in Tab. 3.1.

543 The signals from DCA variations is shown in Fig. 3.27. The difference between
 544 the solid markers and the empty markers are shown in Fig. 3.28. The average of

Cuts	Values
Standard DCA	< 1.0 cm
Tight DCA	< 0.8 cm
Loose DCA	< 1.2 cm
Standard nHitsFit	> 20
Standard nHitsDedx	> 15
Tight Hit Points	nHitsFit > 25, nHitsDedx > 17
Loose Hit Points	nHitsFit > 18, nHitsDedx > 13
Standard $1/\beta$	From Student T fit
Loose $1/\beta$	From Gaussian Fit

Table 3.1 : Cut variations.

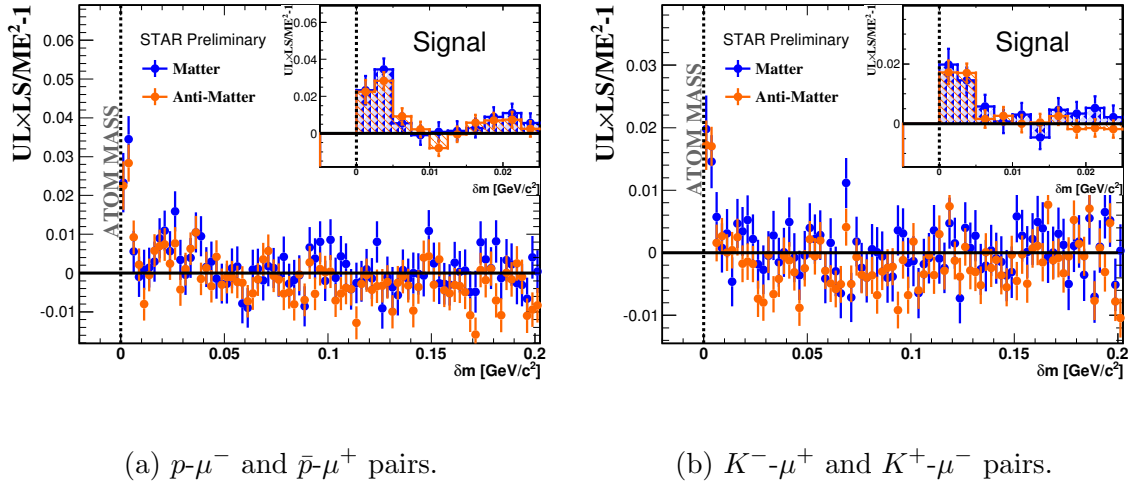


Figure 3.26 : The $UL \times LS/ME^2 - 1$ distributions show peaks at the atom masses.

The x-axis is the mass difference between the pair invariant mass and the sum of hadron and muon mass: $\delta m = m_{pair} - m_{hadron} - m_{muon}$

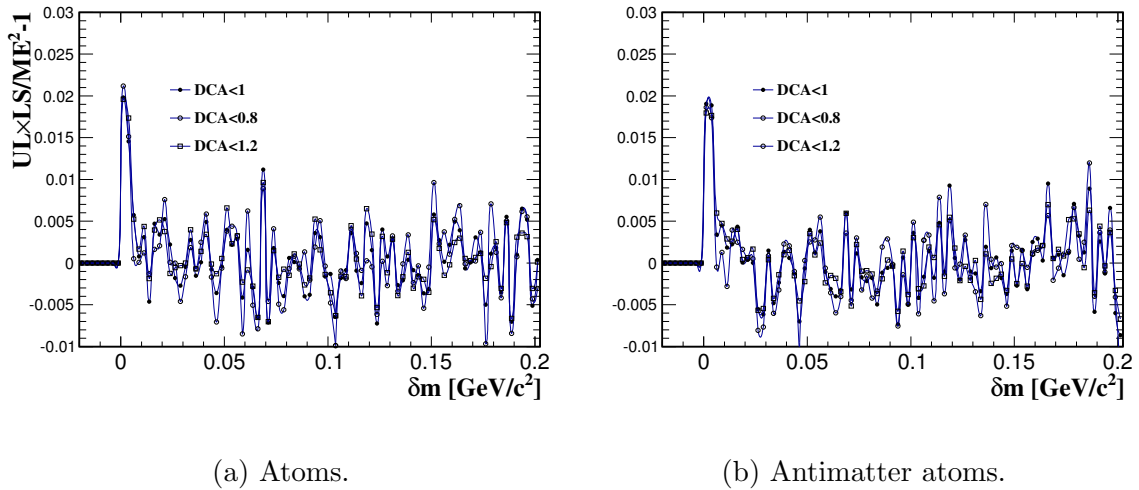


Figure 3.27 : DCA variation.

545 the absolute values of the differences are shown in solid markers and will be quoted
 as systematic uncertainties. The updated plots with systematic errors shown with

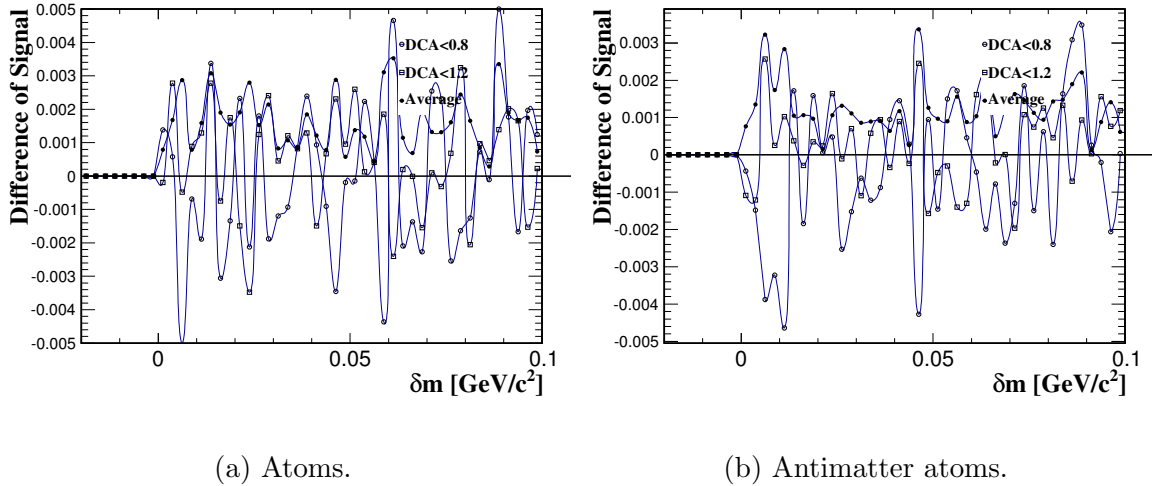


Figure 3.28 : DCA variation.

546

547 gray bands are Fig. 3.29. One can see that the band can well describe how much the
 548 signals change when the DCA cut is varied.

549 Note that the two hit point cuts are highly correlated, i.e. a track with large
 550 nHitsDedx tends to have a large nHitsFit, vice versa. To deal with this positive
 551 correlations, these two cuts were varied at the same time, as shown in Fig. 3.30. The
 552 difference between the solid markers and the empty markers are shown in Fig. 3.31.
 553 The average of the absolute values of the differences are shown in solid markers and
 554 will be quoted as systematic uncertainties.

555 The TOF identification cuts were also varied to study the effect from hadron
 556 contamination. The loose TOF cut was obtained from Gaussian model fits to the

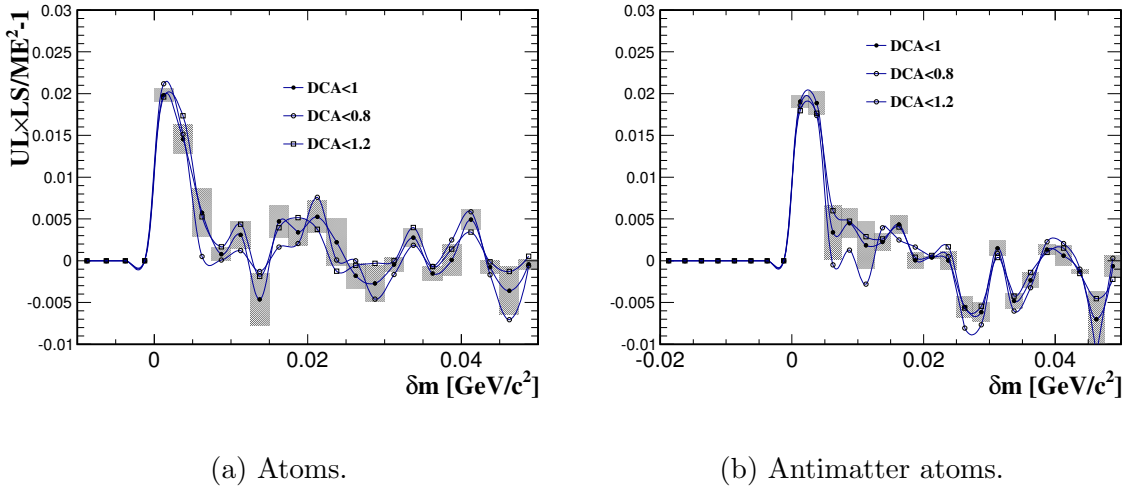


Figure 3.29 : DCA variation.

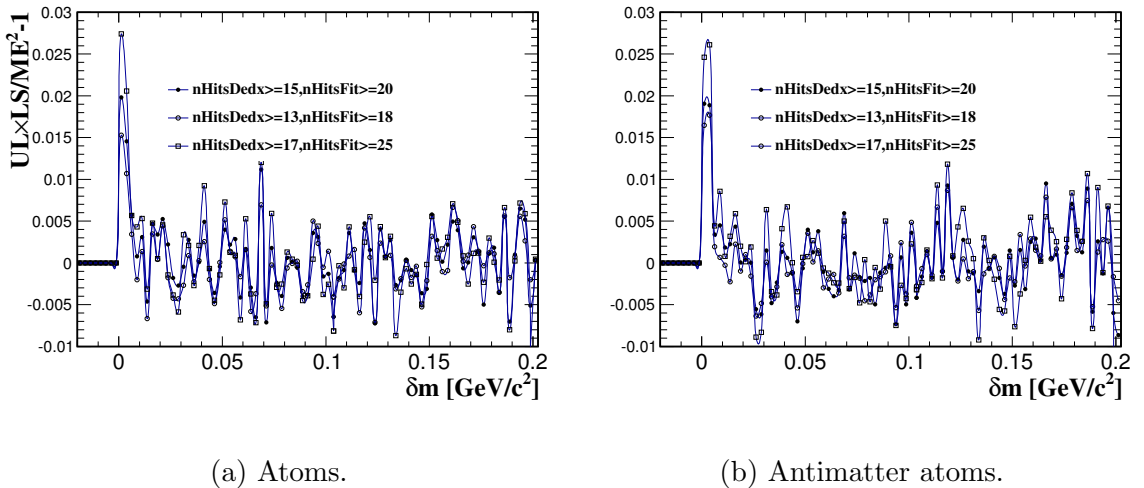


Figure 3.30 : Cuts variation for both nHitsFit and nHitsDedx.

557 $\Delta 1/\beta$ distributions. The Gaussian model has a smaller tail compared to data and
 558 thus will bring in more contamination. The distributions calculated from both cuts
 559 are shown in Fig. 3.32. The differences between the two cuts are shown in Fig. 3.33

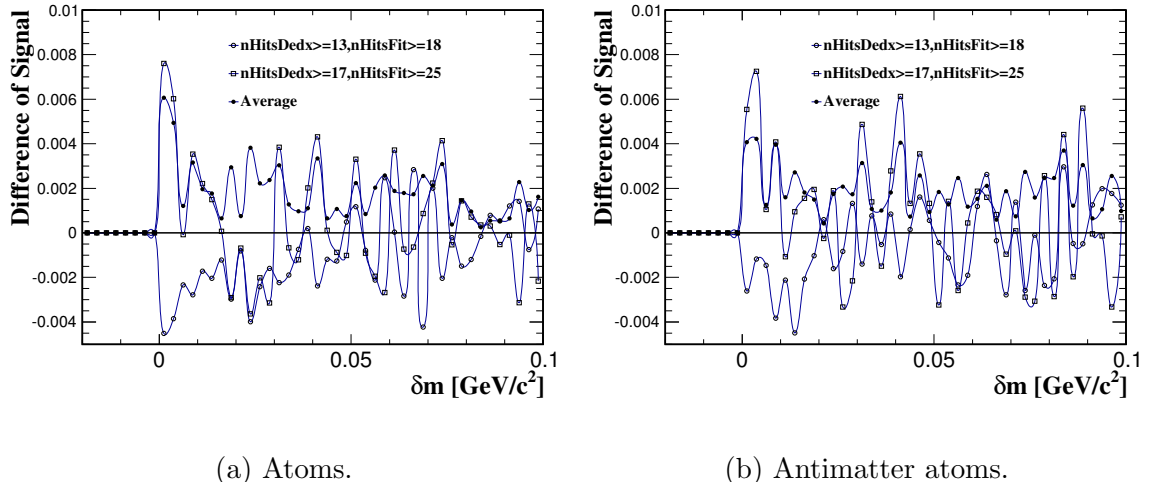
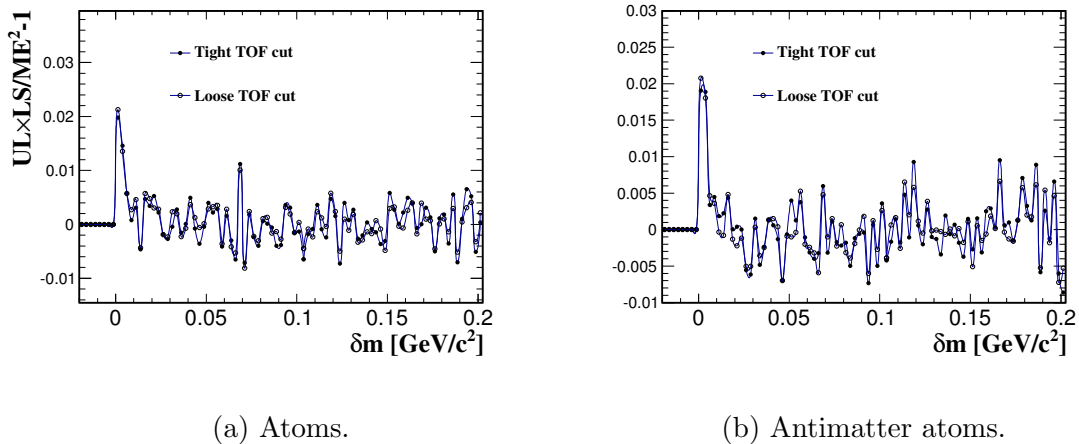


Figure 3.31 : DCA variation.

and will be included in total uncertainty.

Figure 3.32 : Cuts variation for $1/\beta$.

The uncertainties from different variations are then added in quadrature to get the total uncertainty, shown in Fig. 3.34 by the solid circles. The same uncertainty

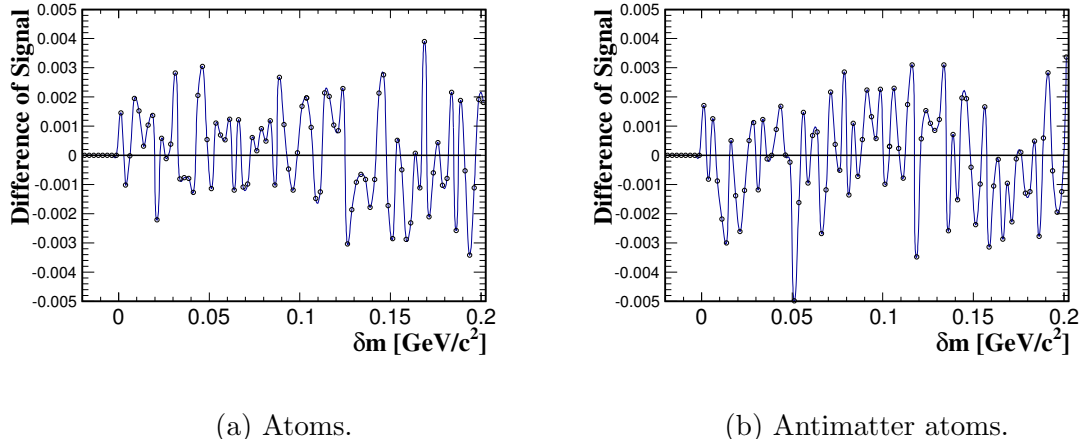
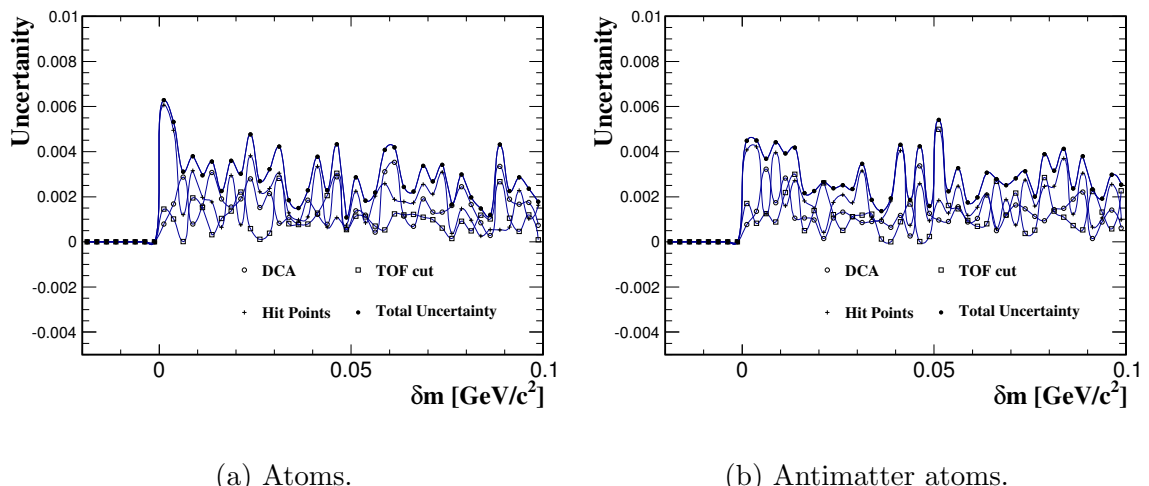
Figure 3.33 : Uncertainties from $1/\beta$ variations.

Figure 3.34 : Systematic uncertainties from all contributions.

563 analysis is performed for antimatter atoms, and the final plots with systematic un-

564 certainties represented by shaded bands are show in Fig. 3.35.

565 Systematic uncertainty study for correlation functions is similar to mass signal.

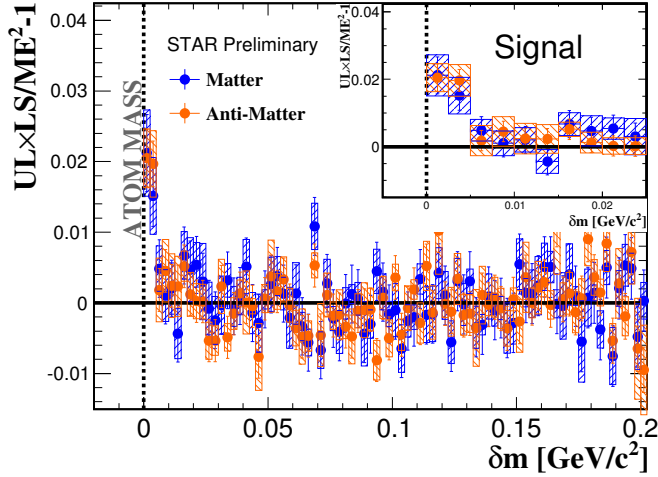


Figure 3.35 : Mass signal, systematic uncertainties represented by shaded bands.

566 An example of the correlation function change from different DCA cuts are shown
 567 in Fig. 3.36. The differences between varied cuts and standard cut are shown in
 568 Fig. 3.37, where the average of the absolute differences are represented by the solid
 569 marks. And other changes from cut variations are shown in Fig. 3.38, Fig. 3.39,
 570 and Fig.3.40.

571 The total relative uncertainties are then added in quadrature: $S_{total} = \sum_i S_i^2$,
 572 where different index represents a different set of cuts. The contributions from each
 573 cuts and the total uncertainties are shown in Fig. 3.41.

574 The absolute uncertainty are plotted as shaded band in Fig. 3.42.

575 The correlation functions for p - π and p - μ pairs are plotted in Fig. 3.43. Due
 576 to limited statistics, no solid conclusion can be drawn for p - μ atoms.

577 The sources of systematic uncertainty for the fraction study are: fitting range,

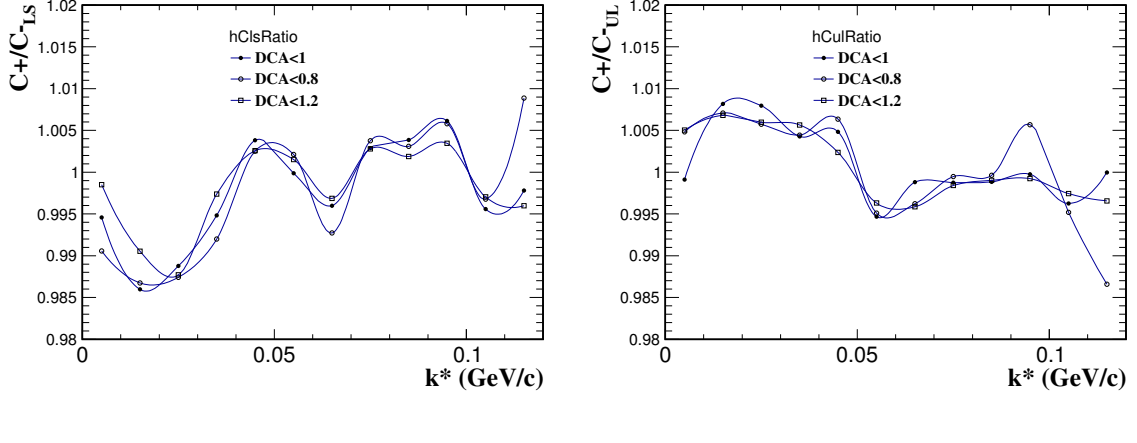


Figure 3.36 : DCA variation.

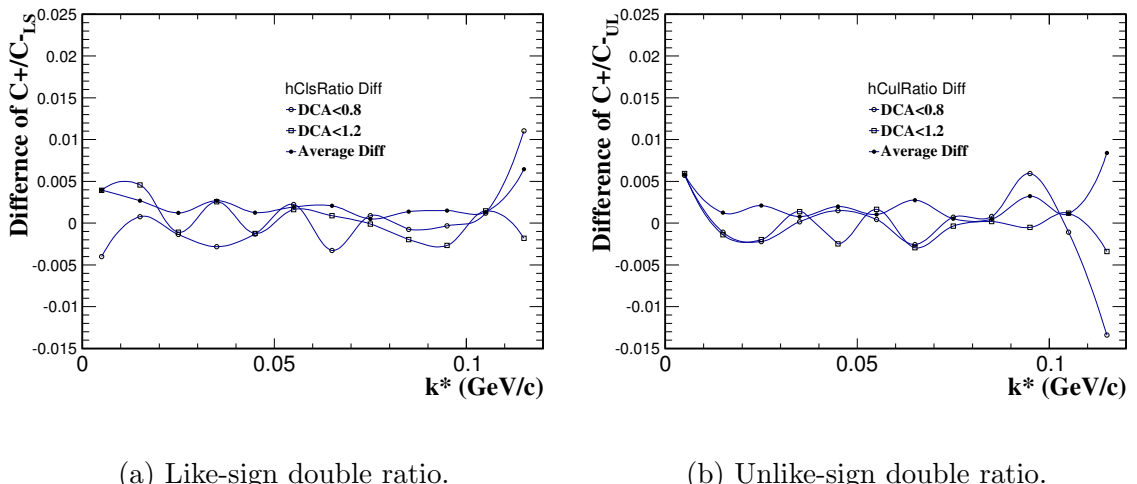


Figure 3.37 : Differences between varied cuts and standard cut.

578 binning effect, and mass difference between the pion and the muon. The fitting range
 579 and binning effect have been shown in Fig. 3.18 and Fig. 3.19. The muon mass
 580 ($105.66 \text{ MeV}/c^2$) is smaller than the pion mass ($139.57 \text{ MeV}/c^2$). The correlation

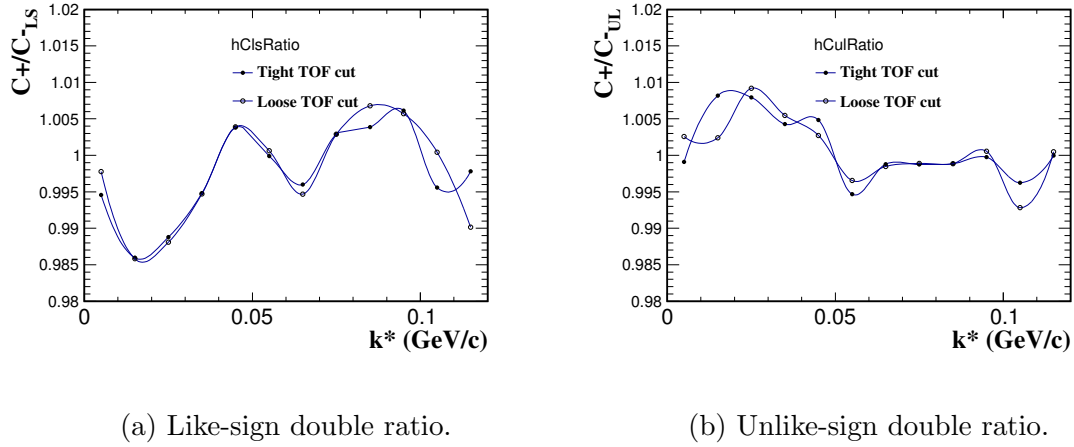


Figure 3.38 : TOF cut variation.

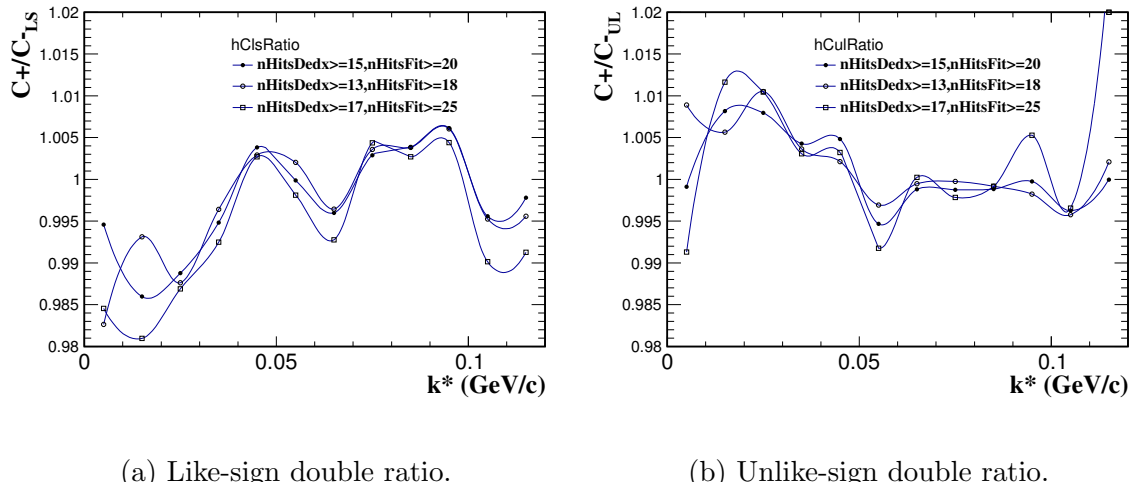


Figure 3.39 : Hit point variation.

function of $\pi - \mu$ would be stronger than $\pi - \pi$ by a factor of the reduced masses of the two systems. This factor is $M_{\pi\pi}^{red}/M_{\pi\mu}^{red} = 1.16$. The data points are first fitted by a function $1-[0]*\exp(-[1]*x)$; then the fit parameters are taken out and set to a

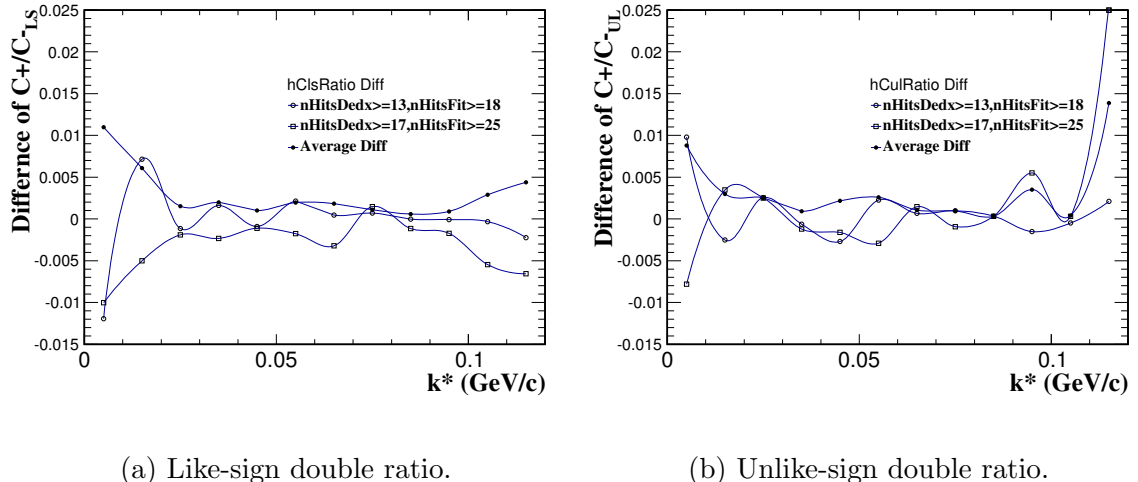
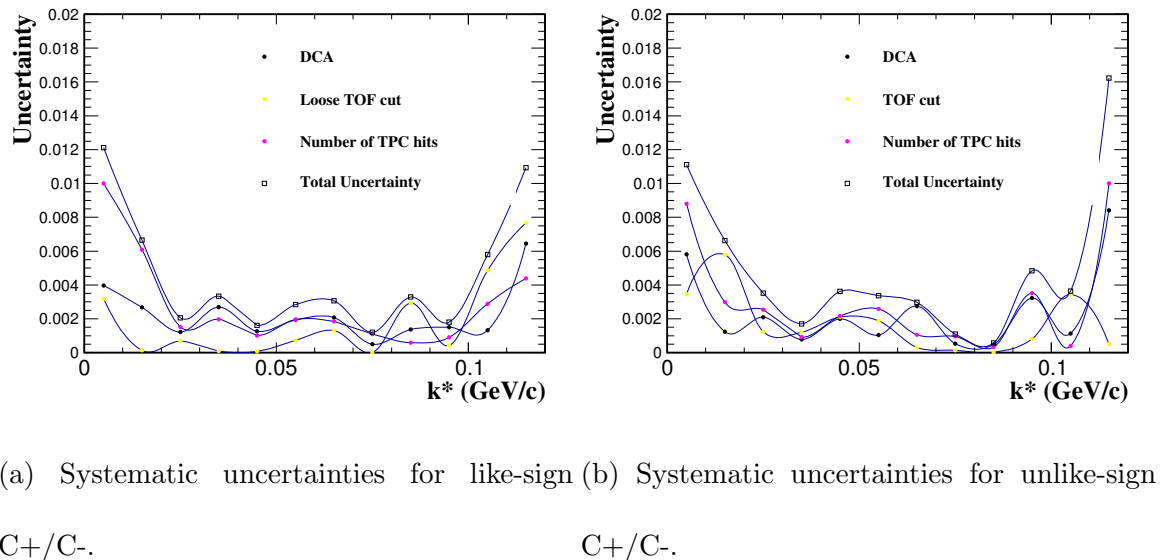


Figure 3.40 : Differences in hit point variation.



(a) Systematic uncertainties for like-sign (b) Systematic uncertainties for unlike-sign
 C_+/C_- .

Figure 3.41 : Total systematic uncertainties are from quadrature sum of contributions.

584 scaled function $1-[0]^*\exp(-[1]^*x^*1.16)$, implying the x-axis is scaled by the reduced
585 mass factor; then a new histogram calculated from the scaled function is used to get

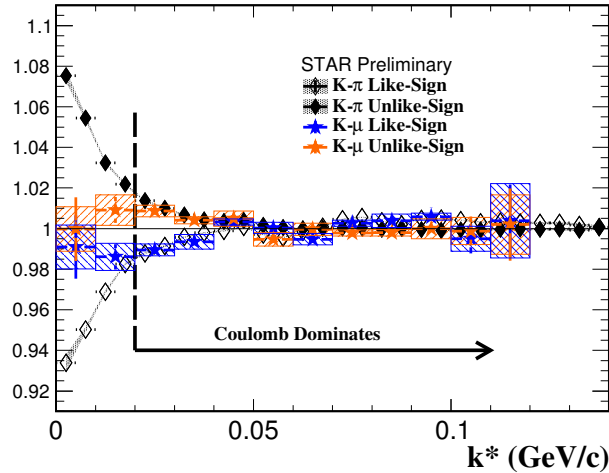


Figure 3.42 : Correlation functions for $K - \pi$ and $K - \mu$ system, systematic uncertainties represented by shaded bands.

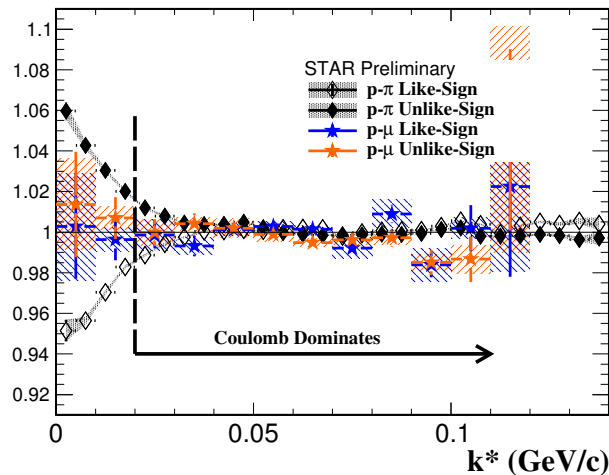


Figure 3.43 : Correlation functions for $p - \pi$ and $p - \mu$ system,.

586 the fitting parameter α . The fitting and scaling functions are shown in Fig. 3.44. The
 587 fitting result with mass scaled correlation function is shown in Fig. 3.45. Combining

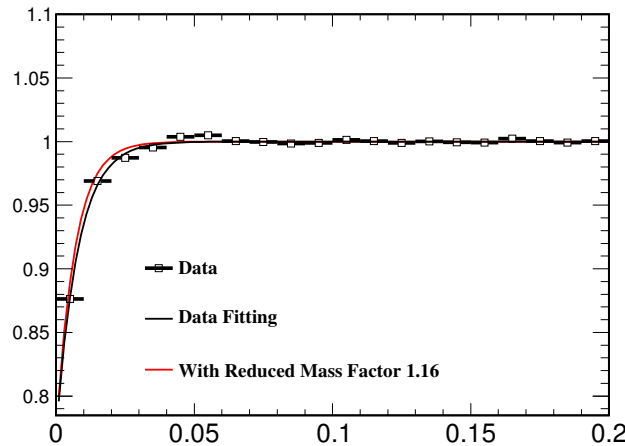


Figure 3.44 : Reduced mass scaling of the correlation function.

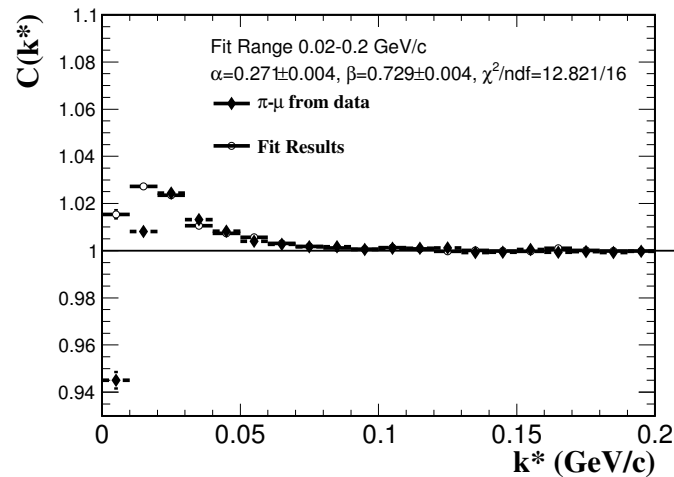


Figure 3.45 : Reduced mass scaling of the correlation function.

588 all these cases, we conclude the fraction of primordial muons is $22.6\% \pm 0.9\% {}^{+0.6}_{-4.5}\%$
 589 %.

590 3.5 Atom Yield from Measurement

591 In this chapter, we count the number of produced atoms from invariant mass study

592 in Section 3.3.

593 The $UL \times LS/ME^2 - 1$ distributions of $K\text{-}\mu$ pairs and $K\text{-}\pi$ pairs are shown in

594 Fig. 3.51. $K\text{-}\pi$ system is flat in most of the signal region, except the first bin. We

595 treat this as the residual from Coulomb cancelation. After the residual is subtracted,

596 the atom signal is shown by the red markers in Fig. 3.51; the antimatter signal is

597 shown by the red markers in Fig. 3.52.

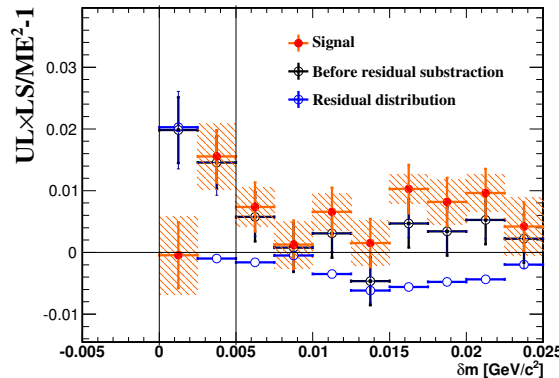


Figure 3.46 : The $UL \times LS/ME^2 - 1$ distribution for atoms from $K\text{-}\pi$ pairs are used as residual background. The atom signal is shown in the shaded area after residual subtraction.

598 Mixed-event has pure combinatorial background and no Coulomb or other inter-

599 actions. The mixed event distributions are shown in Fig. 3.48.

600 The signal is then multiplied by mixed-event to get the atom candidates. $UL \times$

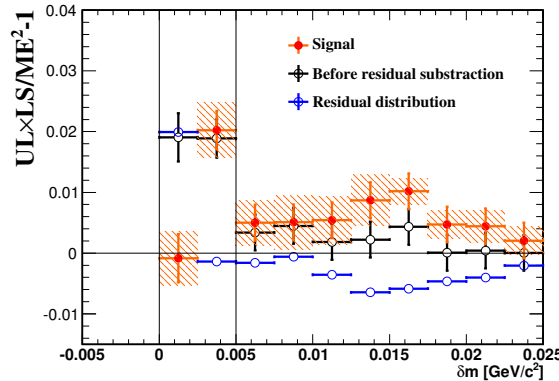


Figure 3.47 : The $UL \times LS/ME^2 - 1$ distribution for antimatter atoms from $K\pi$ pairs are used as residual background. The atom signal is shown in the shaded area after residual subtraction.

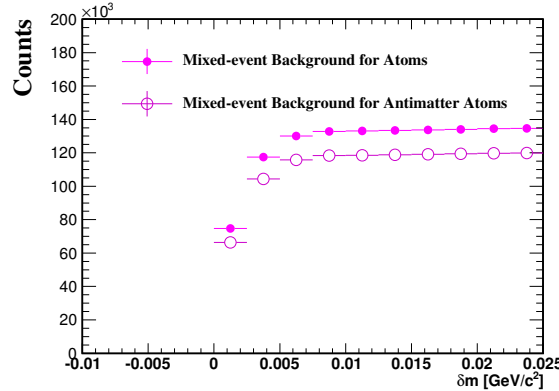


Figure 3.48 : The mixed-event distributions for $K^+\mu^-$ and $K^-\mu^+$.

601 $LS/ME - ME$ represents foreground subtracting background, i.e. the counts of the
602 candidates. The atom and antimatter atom candidates are then shown in Fig. 3.53.

603 The number of $K^+ - \mu^-$ candidates we get from this measurement is $1868 \pm 623 \pm 750$,
604 and the number of antimatter $K - \mu$ candidates is $2125 \pm 412 \pm 537$.

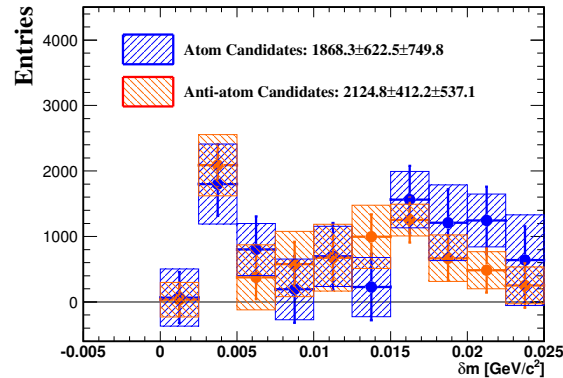


Figure 3.49 : The $K\mu$ atoms and antimatter atom candidates

605 The invariant mass distribution for $p - \pi$ has a peak around net mass $35 \text{ MeV}/c^2$
 (Fig. 3.50), which is due to the Λ baryon decay to a proton and a pion.

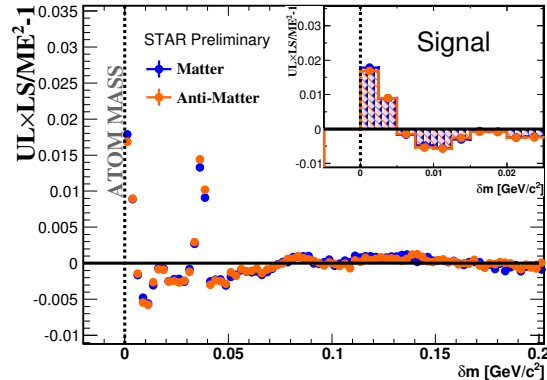


Figure 3.50 : Invariant mass distributions for proton- π pairs.

606
 607 The signal is then multiplied by mixed-event to get the atom candidates. $UL \times$
 608 $LS/ME - ME$ represents foreground subtracting background, i.e. the counts of
 609 the candidates. The atom and antimatter atom candidates are then shown in Fig.

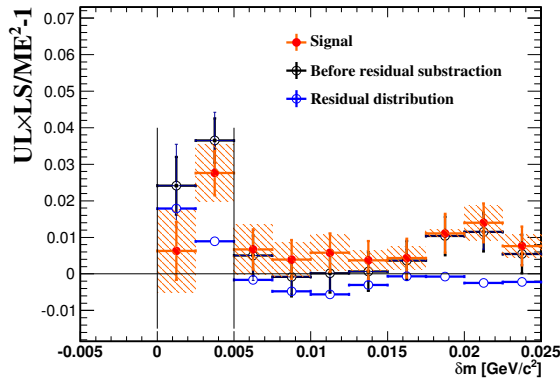


Figure 3.51 : The $UL \times LS/ME^2 - 1$ distribution for atoms from p - π pairs are used as residual background. The atom signal is shown in the shaded area after residual subtraction.

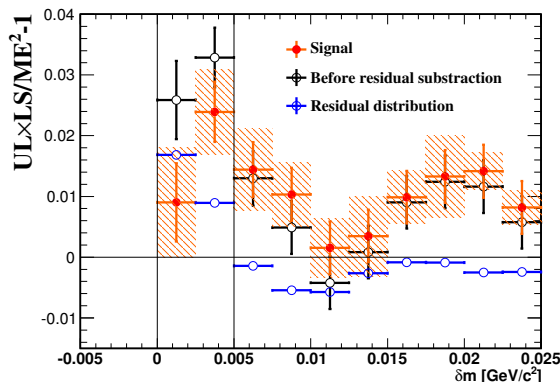


Figure 3.52 : The $UL \times LS/ME^2 - 1$ distribution for antimatter atoms from p - π pairs are used as residual background. The atom signal is shown in the shaded area after residual subtraction.

3.53. The number of muonic hydrogen candidates we get from this measurement

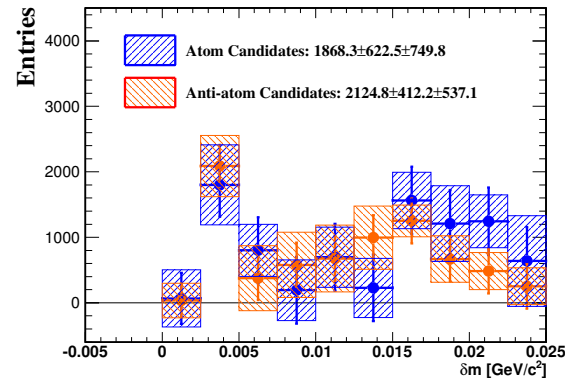


Figure 3.53 : The muonic hydrogen and antimatter muonic hydrogen candidates

610

611 is $1973 \pm 482 \pm 642$, and the number of antimatter muonic hydrogen candidates is

612 $1280 \pm 272 \pm 382$.

613

Chapter 4

614 Theoretical Calculation with Measure Hadron and 615 Lepton Yield

⁶¹⁶ In this chapter, the measured yield from the experiment is used to calculate the
⁶¹⁷ expected yield from theory estimation.

The atom yield can be calculated from the hadron yield and the lepton yield.

Assuming $A_{atom} = a_{atom}/\sqrt{\epsilon_{atom}}$ is the quantum mechanical amplitude of the atom, we get the distribution:

$$dN_{atom} = |A_{atom}|^2 \frac{d^3 p_{atom}}{(2\pi)^3} \quad (4.1)$$

621

$$\frac{dN_{atom}}{d^3p_{atom}} = \frac{1}{(2\pi)^3} |A_{atom}|^2 \quad (4.2)$$

622

$$\frac{d^3 N_{atom}}{dp_x dp_y dp_z} = \frac{d^3 N}{p_t dp_t d\phi dp_z} \quad (4.3)$$

$$= \frac{d^2 N}{2\pi p_t dp_t dp_z} \quad (4.4)$$

$$= \frac{d^2 N}{2\pi p_t dp_t d(m_t \sinh(y))} \quad (4.5)$$

$$= \frac{d^2 N}{2\pi p_t dp_t m_t \cosh(y) dy} \quad (4.6)$$

$$= \frac{d^2 N}{2\pi E p_t dp_t dy} \quad (4.7)$$

$$= \frac{1}{(2\pi)^3} |A_{atom}|^2 \quad (4.8)$$

$$= \frac{1}{(2\pi)^3} \frac{|a_{atom}|^2}{\epsilon_{atom}} \quad (4.9)$$

623 where $a_{atom} = A_{atom} \sqrt{\epsilon_{atom}}$ is Lorentz invariant. We get

$$\frac{d^2 N}{2\pi p_t dp_t dy} = \frac{1}{(2\pi)^3} |a_{atom}|^2 \quad (4.10)$$

624 The joint distribution of hadrons and leptons are given in terms of the amplitude

625 by

$$dN_h dN_\mu = |A_{h\mu}|^2 \frac{d^3 p_h}{(2\pi)^3} \frac{d^3 p_\mu}{(2\pi)^3} \quad (4.11)$$

626 So,

$$\frac{dN_h}{d^3 p} \frac{dN_\mu}{d^3 p_\mu} = \frac{1}{(2\pi)^6} |A_{h\mu}|^2 \quad (4.12)$$

627 The amplitude has the form $A_{h\mu} = a(\vec{p}_h, \vec{p}_\mu)/\sqrt{\epsilon_h \epsilon_\mu}$, where

$$\frac{dN_h}{2\pi \epsilon_h p_T dp_T h dy} \frac{dN_\mu}{2\pi \epsilon_\mu p_T dp_T \mu dy} = \frac{1}{(2\pi)^6} \left| \frac{a(\vec{p}_h, \vec{p}_\mu)}{\sqrt{\epsilon_h \epsilon_\mu}} \right|^2 \quad (4.13)$$

628

$$\frac{dN_h}{2\pi p_T dp_T h dy} \frac{dN_\mu}{2\pi p_T dp_T \mu dy} = \frac{1}{(2\pi)^6} |a(\vec{p}_h, \vec{p}_\mu)|^2 \quad (4.14)$$

629 Take the ratio of equation 4.10 and equation 4.14

$$\frac{\frac{dN_{atom}}{2\pi p_{Tatom} dp_{Tatom} dy}}{\frac{dN_h}{2\pi p_{Th} dp_{Th} dy} \frac{dN_\mu}{2\pi p_{T\mu} dp_{T\mu} dy}} = (2\pi)^3 \frac{|a_{atom}|^2}{|a_{h\mu}|^2} \quad (4.15)$$

630 The amplitude for a hadron and a muon to form an atomic state n and a total
631 momentum \vec{p} is given by

$$A_{atom}(n, \vec{p}) = \sum_{\vec{q}} A_{h\mu}(m_h \vec{p}/m_a + \vec{q}, m_\mu \vec{p}/m_\mu - \vec{q}) \Psi_n^L(\vec{q})^* \quad (4.16)$$

632 Where $\Psi_n^L(\vec{q})^*$ is the Fourier transform of the spatial wave function $\Psi_n^L(\vec{r})$ of the
633 relative coordinate in atomic state n in the laboratory frame, and $m_a = m_\pi + m_\mu$
634 is the rest mass of the atom (neglecting the small binding energy). Considering the
635 relative momenta is small $|\vec{q}| \ll |\vec{p}|$

$$A_{atom}(n, \vec{p}) \approx A_{h\mu}(m_h \vec{p}/m_a, m_\mu \vec{p}/m_\mu) \Psi_n^L(\vec{r} = 0)^* \quad (4.17)$$

636 Note that the collision volume (a few fm) is much smaller than the radius of the
637 atoms (hundreds of fm). Only s-states can be formed with priceable probability.
638 The wave function at the origin in the atom center-of-mass frame with principal
639 quantum number n is given by

$$\psi_n(0) = \psi_n^L(\vec{r} = 0) \sqrt{m_a/\epsilon_{atom}} = (m_{red}\alpha/n)^{3/2}/\sqrt{\pi} \quad (4.18)$$

640 Note that in a hydrogen-like atom, the relative velocity v_{rel} of the hadron and the
641 muon is the Bohr velocity $\alpha c/n$. Thus the relative velocity of the two satisfies $\lesssim ac$.
642 This gives the approximation $\vec{p}_h/\sqrt{p^2 + m^2} \approx \vec{p}_\mu/\sqrt{p^2 + m_\mu^2}$. Thus $\epsilon_h \epsilon_\mu / \epsilon_{atom}^2 =$

⁶⁴³ $m_h m_\mu / m_a^2 = m_{red} / m_a$, we get

$$A_{atom} = A_{h\mu} \frac{(m_{red}\alpha/n)^{3/2}/\sqrt{\pi}}{\sqrt{m_a/\epsilon_{atom}}} \quad (4.19)$$

$$\frac{a_{atom}}{a_{h\mu}} = \sqrt{\frac{\epsilon_{atom}}{\epsilon_h \epsilon_\mu}} \frac{(m_{red}\alpha/n)^{3/2}/\sqrt{\pi}}{\sqrt{m_a/\epsilon_{atom}}} \quad (4.20)$$

⁶⁴⁴ Substitute equation 4.20 into equation 4.15

$$\frac{dN_{atom}}{\frac{2\pi p_{Tatom} dp_{Tatom} dy}{dN_h dN_\mu}} = (2\pi)^3 \frac{\epsilon_{atom}^2 (m_{red}\alpha/n)^3 / \pi}{\epsilon_h \epsilon_\mu m_a} \quad (4.21)$$

$$= 8\pi^2 \frac{m_a^2 (m_{red}\alpha/n)^3}{m_h m_\mu m_a} \quad (4.22)$$

$$= 8\pi^2 m_{red}^2 (\alpha/n)^3 \quad (4.23)$$

⁶⁴⁵ Sum over n to take into account of all states:

$$\frac{dN_{atom}}{2\pi p_{Tatom} dp_{Tatom} dy} = 8\pi^2 \xi(3) m_{red}^2 \alpha^3 \frac{dN_h}{2\pi p_{Th} dp_{Th} dy} \frac{dN_\mu}{2\pi p_{T\mu} dp_{T\mu} dy} \quad (4.24)$$

⁶⁴⁶ where $\xi(3) = \sum_n n^{-3} = 1.202$

$$dN_{atom} = 8\pi^2 \xi(3) m_{red}^2 \alpha^3 \frac{dN_h}{2\pi p_{Th} dp_{Th} dy} \frac{dN_\mu}{2\pi p_{T\mu} dp_{T\mu} dy} 2\pi p_{Tatom} dp_{Tatom} dy \quad (4.25)$$

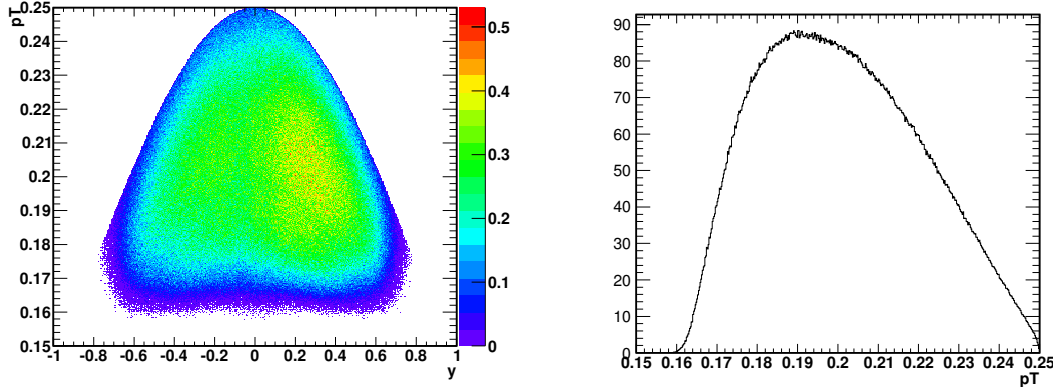
⁶⁴⁷ Use muons and kaons that pass our track selection as input. We can use the

⁶⁴⁸ Eq. 4.25 to get number of atoms. The production on the right-hand side needs to be

649 calculated bin-by-bin. Note that the p_T binning is different for the three distributions.

650 The bin widths are proportional to their masses.

651 First we fill the histogram of p_T v.s. rapidity distribution of negative charged
 652 muons that were identified, weighted by $\frac{1}{2\pi p_{T\mu}}$. The the distribution is scaled by
 653 $N_{event} dp_T dy$ to get the muon factor $\frac{1}{N_{event}} \frac{dN_\mu}{2\pi p_{T\mu} dp_{T\mu} dy}$ shown on the left hand side
 654 in Eq. 4.25. The plot is shown in Fig. 4.1a. There are 500×500 bins in this plot,
 655 within $-1 < y < 1$ and $0.15 GeV/c < p_T < 0.25 GeV/c$. The requirement of each track
 656 having a TOF hit caused the lower boundary around $p_T = 0.16 GeV/c$. The cut on
 657 momentum less than 0.25 GeV/c caused the smooth upper boundary. The projected
 658 plots to p_T is shown in Fig. 4.2b.

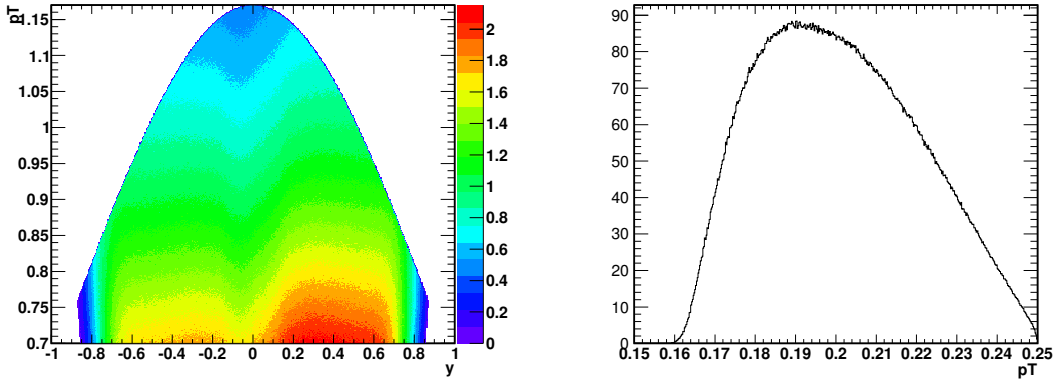


(a) p_T v.s. rapidity distribution of μ^- , (b) p_T distribution of μ^- , weighted by $\frac{1}{2\pi p_{T\mu}}$
 weighted by $\frac{1}{2\pi p_{T\mu}}$.

Figure 4.1 : μ^- phase space, weighted by $\frac{1}{2\pi p_{T\mu}}$.

659 Similarly, K^+ distributions in phase space $\frac{1}{N_{event}} \frac{dN_h}{2\pi p_{Th} dp_{Th} dy}$ is shown in Fig.

4.2a, and its p_T spectra is shown in Fig. 4.2b. The 2D plot in Fig. 4.2a represents the hadron term in Eq. 4.25. There are also 500×500 bins, within $-1 < y < 1$ and $0.7\text{GeV}/c < p_T < 1.17\text{GeV}/c$. Such that in this plot, each individual bin correspond to each bin in the muon distribution in Fig. 4.1a.



(a) p_T v.s. rapidity distribution of K^+ , (b) p_T distribution of K^+ , weighted by weighted by $\frac{1}{2\pi p_{T\mu}}$.

$$\frac{1}{2\pi p_{T\mu}}.$$

Figure 4.2 : K^+ phase space, weighted by $\frac{1}{2\pi p_{T\mu}}$.

The coefficient term in Eq. 4.25 is $8\pi^2\xi(3)m_{red}^2\alpha^3 = 8\pi^2 \times 1.202 \times \frac{m_K m_\mu}{m_K + m_\mu} = 2.793 \times 10^{-7}$.

The last term in Eq. 4.25 $2\pi p_{Tatom} dp_{Tatom} dy$ is determined by the p_T of the atom in current bin, the bin width in the atom histogram, and the rapidity width in the atom histogram. Then at last, bin-by-bin the contents and errors are taken and multiplied by the coefficient calculated above. The results were filled in a new histogram shown in Fig. 4.3a, which is the left term in Eq. 4.25. Note that this histogram is defined

671 with 500×500 bins within $-1 < y < 1$ and $0.85GeV/c < p_T < 1.42GeV/c$. Each bin
 672 correspond to a bin in Fig. 4.1a and Fig. 4.2a.

673 The distribution dN_{atom} is then scaled by N_{event} to get the count distribution
 674 dN_{atom} for atoms, shown in Fig. 4.3a and Fig. 4.3b. The integral over the whole
 675 range give the yield from $K^+ - \mu^-$ atoms: 53.3 ± 0.4 .

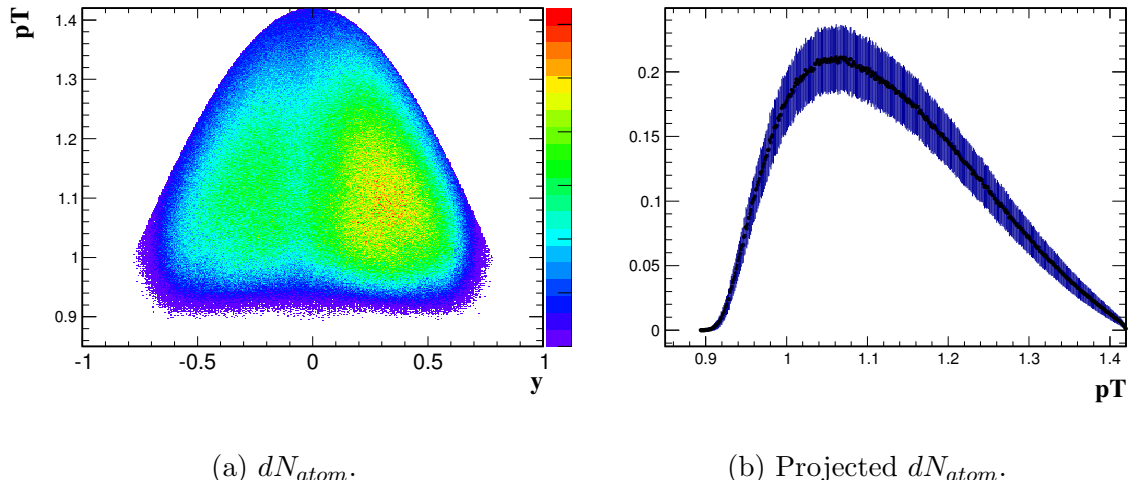


Figure 4.3 : Atom count distributions.

676 Similarly, $dN_{anti-atom}$ is shown in Fig. 4.4a and Fig. 4.4b. The integral over the
 677 whole range give the yield from $K^- - \mu^+$ atoms: 39.0 ± 0.3 .

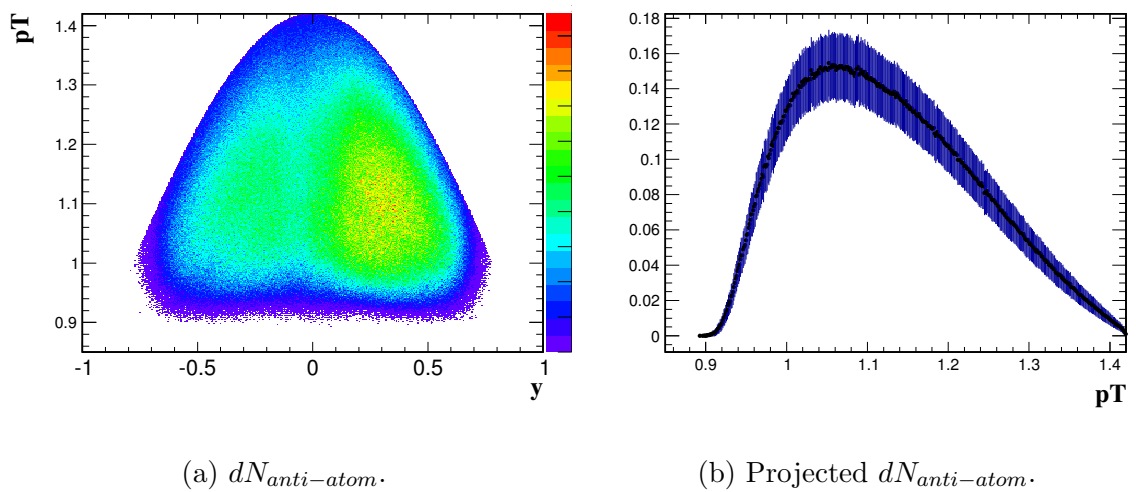


Figure 4.4 : Anti-atom count distributions.

Bibliography

- 678
- 679 [1] Aldo Antognin, *et al.*, Science **339** 417 (2013).
- 680 [2] Y. Tanaka and B. M. Steffen, Phys. Rev. Lett. **51** 18 (1983).
- 681 [3] R. Coombes, *et al.*, Phys. Rev. Lett. **37** 5 (1976).
- 682 [4] S. H. Aronson, *et al.*, Phys. Rev. Lett. **48** 16 (1982).
- 683 [5] G. Baym, G. Freidman, R. J. Hughes, and B. Jack, Phys. Rev. **D48** 9 (1993).
- 684 [6] J. Kapusta and A. Mocsy, Phys. Rev. C **59** 5 (1999).
- 685 [7] A. Adare, *et al.*, Phys. Rev. C **81** 5 (2010).
- 686 [8] L. Adamczyk, *et al.*, Phys. Rev. C **86** 5 (2012).
- 687 [9] J. Adams, *et al.*, Phys. Rev. Lett. **91** 26 (2003).
- 688 [10] J. Adams, *et al.*, Phys. Rev. C **71** 044906 (2005).
- 689